CHALMERS
UNIVERSITY OF TECHNOLOGY

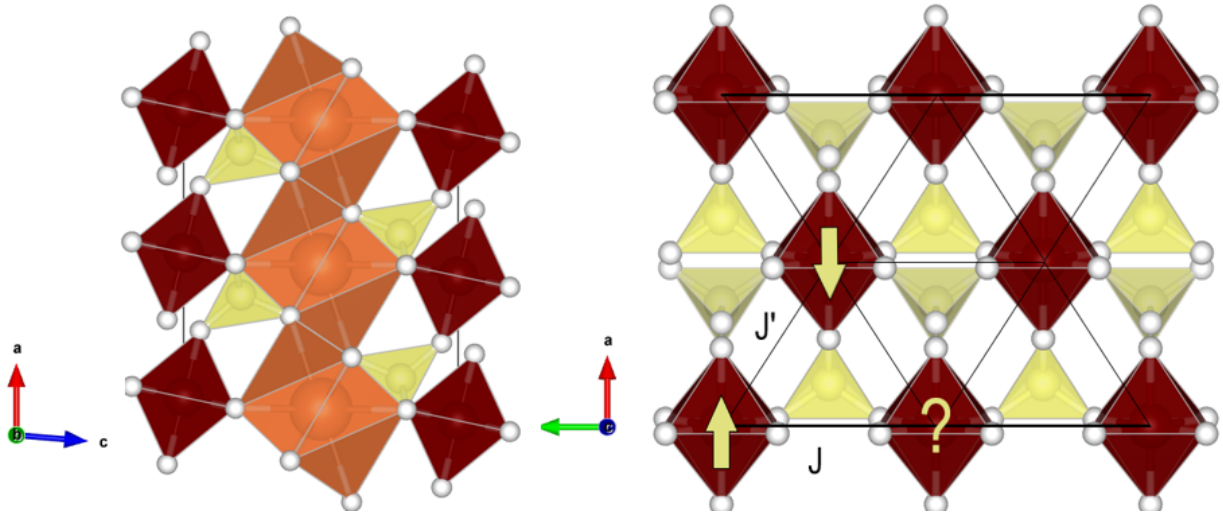

Syntheses, structures, and low-temperature magnetic properties of anhydrous alums

A study on the low-temperature magnetic properties of quantum materials

Master's thesis in Materials Chemistry

ALY ABDELDAIM

Department of Chemistry and Chemical Engineering
CHALMERS UNIVERSITY OF TECHNOLOGY
Gothenburg, Sweden 2018

Master's thesis 2018

Syntheses, structures, and low-temperature magnetic properties of anhydrous alums

A study on the low-temperature magnetic properties of quantum materials

ALY ABDELDAIM

CHALMERS
UNIVERSITY OF TECHNOLOGY

Department of Chemistry and Chemical Engineering
Environmental Inorganic Chemistry
Chalmers University of Technology
Gothenburg, Sweden 2018

Syntheses, structures, and low-temperature magnetic properties of anhydrous alums
A study on the low-temperature magnetic properties of quantum materials
ALY ABDELDAIM

Supervisors:
Gøran J. Nilsen, Polarised neutron scientist, ISIS Neutron and Muon Source, Rutherford Appleton Laboratory, UK
Seikh M.H. Rahman, Post Doc, Chalmers University of Technology, Chemistry and Chemical Engineering, Environmental Inorganic Chemistry, Sweden
Dariusz W. Wardecki, Post Doc, Chalmers University of Technology, Chemistry and Chemical Engineering, Environmental Inorganic Chemistry, Sweden
Examiner:
Sten Eriksson, Chalmers University of Technology, Professor, Chemistry and Chemical Engineering, Environmental Inorganic Chemistry, Sweden

Master's Thesis 2018
Department of Chemistry and Chemical Engineering
Environmental Inorganic Chemistry
Chalmers University of Technology
SE-412 96 Gothenburg
Telephone +46 31 772 1000

Cover: (a) $AB(XO_4)_2$ projected on the a-c plane. (b) $AB(XO_4)_2$ projected on the a-b plane, where A cations are omitted for clarity in viewing the triangular sheets. BO_6 octahedra are presented in red, XO_4 tetrahedra are in yellow, and BaO_{10} bi-capped square anti-prisms are in orange. The structure was generated using the VESTA visualization software [1]. Yellow arrows are present to illustrate geometrical frustration on triangular motifs

Printed by Reproservice Chalmers
Gothenburg, Sweden 2018

New model magnets in the anhydrous alum family
A study of geometrically frustrated antiferromagnets
ALY ABDELDAIM
Department of Chemistry and Chemical Engineering
Chalmers University of Technology

Abstract

In this thesis, anisotropic triangular systems belonging to the anhydrous alum family are studied. A Mo^{4+} $S = 1$ system in the form of $BaMo(PO_4)_2$ is first presented. Crystallographic determination is carried out using X-ray and neutron powder diffraction studies. Low-temperature magnetic properties are reported by analyzing magnetic susceptibility, specific heat, low temperature neutron powder diffraction, and neutron spectroscopy data. An effective one dimensional Ising Neél state is predicted from the data.

Further presented are a continuation of a series of $S = 1/2$ Ti^{3+} systems. Those follow the formula $ATi(SO_4)_2$ (A=Rb,Cs) and are studied as a continuation of previously reported $KTi(SO_4)_2$ [2]. Powder X-ray diffraction is utilized in crystallographic determination. Magnetic susceptibility and specific heat measurements are carried out, and susceptibility analytical expressions for the spin Hamiltonian are used to fit the data. Excellent agreement between collected and fitted data is observed, and a one-dimensional Heisenberg chain is suggested. A trend of increasing one-dimensionality is noted with increasing ionic radius.

Magnetic susceptibility, specific heat, and low-temperature neutron powder diffraction data for $NaFe(SO_4)^2$ are reported in the Appendix.

Keywords: Low-temperature, magnetism, geometrical frustration, anhydrous alum

Acknowledgements

Undoubtedly, the following work is a representation of the combined efforts of many talented individuals I am privileged to have worked with, even if the prose is written by myself. First and foremost, for the patience and kindness in guiding me through a subject I began knowing nothing about, I would like to give my sincerest gratitude to my supervisor Dr. Gøran Nilsen. While there is still so much left to learn, the appropriate building blocks are well grounded. Thank you for sharing your knowledge, your enthusiasm was often my source of motivation. I would also like to extend my appreciation to my co-supervisors Dr. Seikh M. H. Rahman and Dr. Dariusz Wardecki for always keeping an open door for any questions and always providing support and positive criticism. Many thanks for Dr. Paul Henry and Nico Torino for their guidance and intriguing discussions.

As for Dr. Sten Eriksson, you have provided the friendliest academic environment for good science to flourish. For endless support on all issues, whether scientific or not, thank you. Your presence have always been a privilege.

Most of the data collected for the current study were acquired at the ISIS Neutron and Muon Source, Didcot, UK, which would have not been possible without the continual aid provided by many skilled scientists. I would like to thank Dr. Gavin Stenning for help on the MPMS and PPMS instruments in the Materials Characterization Laboratory. For support and access to beam time, I am grateful to Dr. Helen Walker and Dr. Alexandra Gibbs for their support on the MERLIN and HRPD instruments, respectively. I would like to extend this gratitude to Dr. Dmitry Khalyavin, Dr. Pascal Manuel, and Dr. Fabio Orlandi for their assistance on the WISH instrument.

Special thanks to all my friends and colleagues at the Inorganic Environmental Chemistry department at Chalmers University of Technology who have made my time here enjoyable. Working on this would not have been the same without all the lunchtimes and fika breaks.

Finally, I am grateful for all the love and unconditional support from my family.

Aly Abdeldaim, Gothenburg, June 2018

Contents

List of Figures

List of Tables

1

Introduction

1.1 Historical Overview

While its first account is historically debatable, magnetism is one of the earliest physical phenomena examined, dating back to the antiquity of Greek legends. A scientific formalism of magnetism did not follow, however, until the early-seventeenth century, predated by explanations invoking myths of other-worldliness in the realm of metaphysics. While it is historically noted that previous scientific attempts existed, most notably by the French physicist Petrus de Maricourt, it is William Gilbert that is credited to be the father of studies on early magnetism. In Gilbert's treatise on magnetism De Magnete, experiments on Fe_2O_3-Fe_3O_4, known as lodestone, were presented as to denounce previous misconceptions and introduce various concepts including the earth's magnetism and the distinction between magnetism and electricity. Nonetheless, the origin of magnetism remained unexplained.

By the beginning of the nineteenth century, the scientific formalism and understanding of magnetism began to take shape. As this occurred in an intertwined fashion between a breadth of scientific contributions, what follows is a non-exhaustive list of several critical experiments in modern magnetism. Laying foundation to the classical theory of electromagnetism, Hans Christian Ørsted was the first to systematically note the deflection of a magnetic compass by an applied current in 1820, thus identifying a connection between electricity and magnetism through the experiment depicted in figure 1.1. This commenced a plethora of scientific contributions from the likes of André-Marie Ampére, Hendrik Lorentz, and Micheal Faraday, combined eventually by James Clerk Maxwell into a set of equations, which, along with the Lorentz force, define the classical theory of electromagnetism.

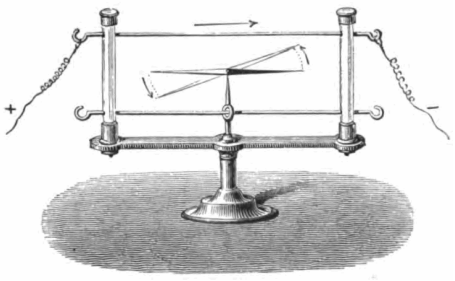

Figure 1.1: Ørsted's original experiment linking electricity to magnetism by noting the deflection of the illustrated compass needle when a current passes in the wire.

The turn of the twentieth century brought with it developments that fueled our current understanding of modern magnetism. After the discovery of the electron in 1897 by Sir J.J. Thomson, the electron's role in magnetic behavior was established. Around the same time, the thermal behavior of magnets, and the critical transition from a symmetrical to a non-symmetrical phase was formalized by Pierre Curie into what is now known as the Curie law. This was later modified by Pierre Weiss, which introduced a fictitious "molecular field" as to explain magnetic ordering within materials, forming the Curie-Weiss law. A fundamental change of the understanding of magnetism followed as quantum mechanics was introduced and embraced. The quantum nature of magnetism was established as the concepts of spin, exchange interactions, and many others were introduced. Modern magnetism began to take shape, with many translations from classical to quantum formalized by John Hasbrouck Van Vleck.

As the theory of magnetism further developed, its scientific presence flourished. Recent years have seen an expanding interest in magnetism in a wide scope ranging medical sciences, electronics, data storage devices, cosmology, and fundamental condensed matter physics, to name a few. Within the field of condensed matter sciences, magnetic materials provide an excellent playground to explore novel quantum phenomena, in particular those arising from strong electron correlations[3]. One manifestation of such materials are quantum spin liquids (QSLs), a class of magnetic materials where, unlike the familiar states of magnetic order, electron spins remain dynamic down to absolute zero in temperature, fluctuating in a correlated manner [4]. While analytically challenging, a breadth of exotic phenomena such as fractional quantum numbers [5], with potential promising applications in quantum computing [6] and memory devices [7], drive the interest in exploring QSLs.

While in search for a realization of the QSL state, frustrated lattices are some of the most prominent candidates. In this context, magnetic frustration generally refers to a state of competing interactions between magnetic moments, where the satisfaction of all interactions is unachievable by any spin configuration [5]. One way frustration can be fulfilled in materials is exemplified by geometrically frustrated lattices, where frustration emerges from the spatial positions of the magnetic atoms [5]. This results in the adoption of exotic ground states of large degeneracy, one of which could be a realization of the QSL state [8]. Geometrically frustrated lattices can be found in naturally occurring minerals or engineered in more complex crystallographic arrangements.

1.2 Objective of the Study

This study extends on the work done on materials belonging to the anhydrous alum family, characterizing their structures and low temperature magnetic properties. The anhydrous alums are chosen as they exhibit a breadth of magnetic topologies. In this study, $BaMo(PO_4)_2$ (BMP), $RbTi(SO_4)_2$ (RTS), $CsTi(SO_4)_2$ (CTS), and $NaFe(SO_4)_2$ (NFS) will be studied. A major part of this thesis will be dedicated towards solving the magnetic structure and spin Hamiltonian of BMP.

This thesis will be structured as to first present in Chapter 2 a brief theoretical background on concepts useful for understanding later discussions. This is by no means a comprehensive discussion, and the interested reader is referred to Mattis [9], Cullity [10], Blundell [11], and Carlin [12] as excellent sources for an overview on magnetic materials. Chapter 3 explains the methodology followed with the experimental techniques applied in this study. Data from magnetometry, specific heat measurements, and elastic and inelastic neutron scattering are examined in Chapter 4 and used to provide discussions on the suggested magnetic models the studied materials exhibit. Finally, the conclusion is discussed in Chapter 5.

2

Theory

2.1 Magnetism

2.1.1 Origin of the Magnetic Moment

The magnetic moment of an atom can be attributed to the angular momentum of its electrons. Total angular momentum **J** of an electron is comprised of two components, the orbital **L** and intrinsic (or spin) **S** angular momenta, and is given as:

$$\mathbf{J} = \mathbf{L} + \mathbf{S} \tag{2.1}$$

Its first contributing component L can be easily pictured by considering Bohr's atomic model where an electron circuits a nucleus in circular orbits as illustrated in figure 2.1.

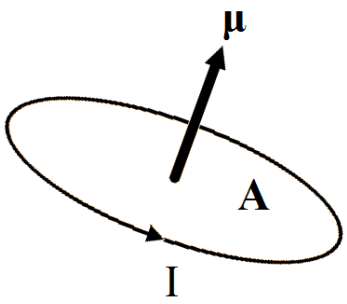

Figure 2.1: Magnetic moment as a result of an orbiting electron current.

This results in a magnetic moment μ that can be simply expressed in terms of the current I and the area of the orbital A such that:

$$\mu_{\mathbf{L}} = I\mathbf{A} \tag{2.2}$$

The orbital angular momentum **L** can be directly related to the magnetic moment where m_e is the mass of an electron, v is its velocity, and r is the radius of the orbital:

$$\mathbf{L} = m_e\mathbf{vr} \tag{2.3}$$

If one considers a current $I = q_e v/2\pi r$ defined by the charge of an electron q_e in a circular area, the magnetic moment according to equation 2.3 is [10]:

$$\mu_{\mathbf{L}} = \pi \mathbf{r}^2 \left(\frac{q_e \mathbf{v}}{2\pi \mathbf{r}} \right) = \frac{q_e \mathbf{v}\mathbf{r}}{2} \tag{2.4}$$

Combining equation 2.3 and 2.4, the relation between orbital angular momentum and the magnetic moment is given by:

$$\mu_{\mathbf{L}} = \frac{q_e}{2m_e}\mathbf{L} \tag{2.5}$$

Energy quantization must be considered in equation 2.5 as both the magnitude and projection of $\mathbf{L}$ are quantized in integer n multiples of $\hbar$ where $\hbar = \frac{h}{2\pi}$ and h is Planck's constant. By combining $\mathbf{L} = n\hbar$ for n=1 and equation 2.5, an essential unit when expressing magnetic moments is the Bohr magneton μ_B described as:

$$\mu_B = \frac{q_e \hbar}{2m_e} = 9.274 \times 10^{-24} Am^2 \tag{2.6}$$

The second component of $\mathbf{J}$ is the intrinsic angular momentum $\mathbf{S}$ known as spin. With no classical counterpart, the conceptualization of spin is unintuitive, and it is left for the reader to consult any of the many books on quantum mechanics for further discussions on its properties.

Finally, with knowledge of the total angular momentum $\mathbf{J}$, the net magnetic moment is expressed as the effective moment μ_{eff}, a commonly measured experimental property defined in terms of [10]

$$\mu_{eff} = g_J \sqrt{J(J+1)} \mu_B \tag{2.7}$$

where J is the total angular momentum quantum number and g_J is a constant calculable from the quantum numbers defining the wavefunction of the electron.

2.1.2 Magnetism in Materials

A magnetic material is comprised of many magnetic atoms or ions, and their interactions give rise to interesting phenomena. Consider an applied magnetic field $\mathbf{H}$ in empty space, the magnetic flux density $\mathbf{B}$ through the permeability of empty space μ_o is unaffected and given as:

$$\mathbf{B} = \mu_o \mathbf{H} \tag{2.8}$$

If a magnetic material occupies the space where a field is applied, its magnetization $\mathbf{M}$, which is the sum of the magnetic moment per unit volume, affects the flux density such that:

$$\mathbf{B} = \mu_o (\mathbf{H} + \mathbf{M}) \tag{2.9}$$

A useful measure of the effect of $\mathbf{H}$ on the magnetization of a material is the magnetic susceptibility χ, most commonly divided by the number of moles n, and reported as the molar susceptibility χ_n:

$$\chi_n = \frac{\mathbf{M}}{\mathbf{H}n} = \frac{\chi}{n} \tag{2.10}$$

Intrinsic to all matter is a property known as diamagnetism which occurs in atoms with filled electronic shells [13]. The effect of diamagnetism is small with temperature independent susceptibilities ranging -10^{-6} emu (electromagnetic unit) mol^{-1} [12] (1 emu mol^{-1}=$4\pi\times10^{-6}$ m^3 mol^{-1}) and can be viewed as a negative magnetization such that the flux density decreases as illustrated in figure 2.2a. On the other hand, if the density of the magnetic flux rises upon applying a magnetic field (figure 2.2b), the material is said to be paramagnetic. Paramagnetism occurs in materials with unpaired electron spins [13] and has a relatively larger effect on the total susceptibility of a magnetic material in orders of 10^{-3} to 10^{-1} emu mol^{-1}.

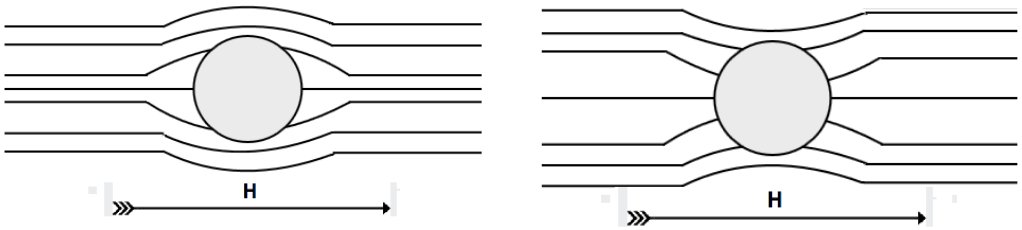

(a) Diamagnetism (b) Paramagnetism

Figure 2.2: Inserting a (a) diamagnetic or a (b) paramagnetic material in an applied field decreases or increases the magnetic flux density, respectively.

Unlike diamagnetism, paramagnetism is temperature dependent, and the simplest model used to describe this dependency is the Curie law given as

$$\chi = \frac{C}{T} \tag{2.11}$$

where C is the Curie constant and T is the temperature. The Curie law encompasses the temperature dependence of paramagnets which can be understood in a simplified picture as follows. When an external field is applied, the randomly oriented magnetic moments within the material orient towards direction of the field, thus increasing the observed magnetization. The thermal energy acts as to counteract this orientation by randomizing the spins.

When using the Curie law, one assumes that no interactions between atoms or ions occur. This makes it an idealized law, and many materials deviate from this behavior. The Curie-Weiss law is a modified version that takes into account moment interactions by introducing a molecular field acting in addition to the applied field and is given as:

$$\chi = \frac{C}{T - \theta_w} \tag{2.12}$$

where θ_w is called the Weiss constant expressed in units of temperature. At relatively low temperatures, the energy associated with magnetic moment interactions becomes comparable to or bigger than the entropy of the system. This implies that at a specific temperature, the system's preferred minimum energy equilibrium can transition from a disordered entropic spin state (e.g. paramagnetic) into an ordered one based on the type of interactions. For long range ordering in which

spin interactions span the whole system, the system transitions into one of the spin states illustrated in simplified forms in figure 2.3 below the Curie temperature T_C, whose temperature behaviors are given in figure 2.4. In simple mean field theory, $T_c = \theta$. However, some systems may not exhibit long range order; instead, short range interactions dominate even at low temperatures as discussed further on.

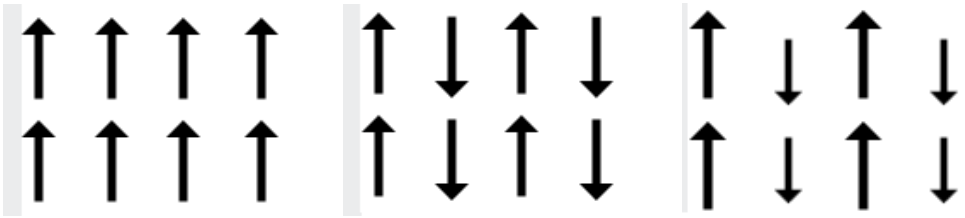

(a) Ferromagnetic (b) Antiferromagnetic (c) Ferrimagnetic

Figure 2.3: Possible long range ordered spin states.

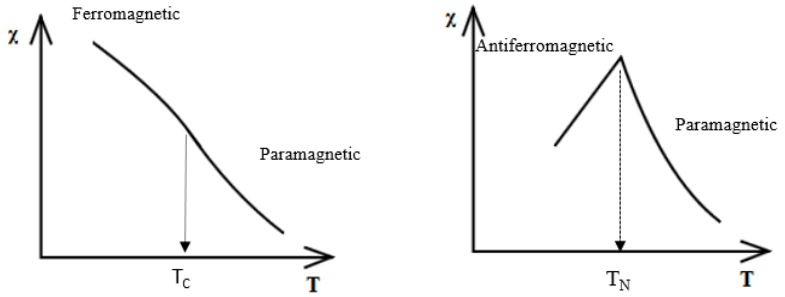

(a) Ferromagnetic (b) Antiferromagnetic

Figure 2.4: A clear transition from a paramagnetic to a (a) ferromagnetic and (b) antiferromagnetic ordered states can be observed from their thermal behavior.

Long-range magnetic ordering is not limited to the simple FM or AFM states. Instead, magnetic moments can form more complicated structures such as conical and cycloidal waves as seen in figure 2.5. The spins can be commensurate (in phase) or incommensurate (out of phase) with respect to the chemical unit cell. Given the periodicity of a unit cell, one can use a propagation vector $\boldsymbol{\kappa}$ to define the propagation of magnetic moments [14]. The distribution of magnetic moments can be expressed as a Fourier series using this vector:

$$\boldsymbol{\mu}(\mathbf{r_n}) = \sum_{\kappa} \mathbf{m}_\kappa \exp(-2\pi i \boldsymbol{\kappa} \cdot \mathbf{r_n}) \tag{2.13}$$

where $\mu(\mathbf{r_n})$ is a magnetic moment of the n-th magnetic atom in a crystal, and $\mathbf{m}_\kappa$ are Fourier coefficients. In the simplest case of a one dimensional crystal with a lattice parameter a, and $\kappa = (1/2, 0, 0)$, eq 2.13 is simplified to

$$\boldsymbol{\mu_n} = \boldsymbol{\mu_0} \cos(n\pi) = \boldsymbol{\mu_0}(-1)^n \tag{2.14}$$

where the coefficient $\mathbf{m}_\kappa$ from eq 2.13 can be identified as a magnetic moment $\boldsymbol{\mu_0}$ at n-th position. In this case, equation 2.14 then describes antiferromagnetic

ordering. In general, however, $\mathbf{m}_\kappa$ can be complex when the magnetic order is non-centrosymmetric.

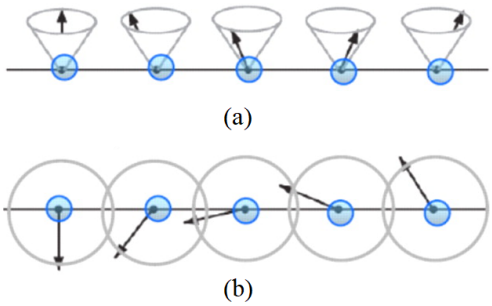

Figure 2.5: Possible long-range ordering on a 1-D lattice where illustrated are (a) conical and (b) cycloidal arrangements. Picture obtained from [15].

2.1.2.1 Interactions

In explaining long-range ordering, the Curie-Weiss law introduces a fictious molecular field to account for all electronic and magnetic interactions. The principle underlying the molecular field was introduced by the exchange energy J, a quantum mechanical term with no classical counter part described in a many body system by the Heisenberg spin Hamiltonian as

$$\mathcal{H} = \sum_{i,j} J_{ij} \mathbf{S}_i \cdot \mathbf{S}_j \tag{2.15}$$

where $\boldsymbol{S_{ij}}$ are spin operators for the ith and jth nearest neighbouring ions. Fundamentally, exchange interactions are electrostatic Coulomb interactions arising between spatially overlapping electron wave functions [16]. They arise due to the Pauli exclusion principle which forbids two electrons in an identical quantum state from occupying the same energy level [16]. This constrains the total wave function of two interacting electrons

$$\Psi(\mathbf{a}, \mathbf{b}) = \Psi(\mathbf{r_1}, \mathbf{r_2}) \chi(\mathbf{s_1}, \mathbf{s_2}) \tag{2.16}$$

to be antisymmetric, which can only occur if its spatial $\Psi(\mathbf{r_1}, \mathbf{r_2})$ and spin $\chi(\mathbf{s_1}, \mathbf{s_2})$ components have opposite symmetry; symmetric and antisymmetric or vice versa. Thus J is associated with the energy differences between the electron quantum states [16], and hence the Coulomb energy, where a positive J indicates a favored antiparallel and thus antiferromagnetic (AFM) spin arrangement, whereas a negative J favors a parallel ferromagnetic (FM) spin state [10].

Usually, however, magnetic ions are placed in a lattice such that they are too far apart for electorn wave functions to overlap directly. Spin ordering can still occur through exchange interactions mediated by orbital overlap with non-magnetic ions such as O^{2-} [11]. This type of interaction is called superexchange and a simplified mechanism is depicted in figure 2.6 where the delocalization of electrons over the metal-oxygen-metal results in an energetically favorable state [11]. The type of interactions resulting from superexchange is governed by the empirical Goodenough-Kanamori rules, and more often than not result in antiferromagnetic exchange [10].

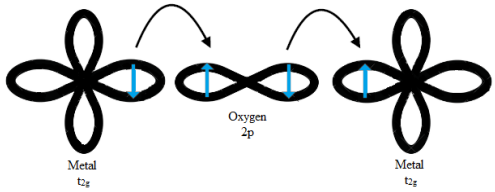

Figure 2.6: Antiferromagnetic 180° super exchange interaction. Potential energy is minimized if the hopping of an electron is permitted as shown.

The permitted direction of the magnetic moments is dependent on the relative strengths of the the crystalline field and spin-orbit interaction [17]. The interaction between spin and orbital momenta is termed spin-orbit (LS) coupling. Its strength (given in terms of the coupling parameter ζ) depends on the electronic structure of the magnetic ion, and increases the heavier an element is [17]. As such, for the materials discussed in this thesis, the effect of LS coupling is expected to be more pronounced for Mo^{4+} ($\zeta = 950\ cm^{-1}$) than for Fe^{3+} ($\zeta = 280\ cm^{-1}$) and Ti^{3+} ($\zeta = 154\ cm^{-1}$) [12].

The strength of LS coupling determines the degree of the orbital angular momentum quenching, which describes the reduction of the orbital moment on non-degenerate electronic configurations. Weak LS coupling, relative to the crystal field, typically results in full orbital angular momentum quenching. When LS coupling is present, it can result in anisotropy, which directly translates into the direction of the magnetic moments as unlike **S**, the orbital angular momentum can be anisotropic [18]. Depending on the properties of the ion considered, this can result in single-ion anisotropy, where magnetization requires less energy along a principle crystallographic axis/axes. This can be captured in the following Hamiltonian

$$\mathcal{H} = D\hat{S}_z^2 + E(\hat{S}_x^2 - \hat{S}_y^2) \tag{2.17}$$

where $\hat{S}_i$ is a spin operator and E is termed the rhombic single ion anisotropy parameter [19]. This Hamiltonian describes both orthorhombic ($|D| > 0\ |E| > 0$) and tetragonal ($|D| > 0\ |E| = 0$) cases, where the symmetry refers to that of the electric field of the ions surrounding the atom, the crystal field. For the tetragonal case, depending on the sign of D, the anisotropy can be either easy axis (Ising) or easy plane (XY).

The strength of the single-ion anisotropy largely depends on the comparative strength of the LS coupling and the crystal field. This can be qualitatively expressed as $D \sim \lambda^2/A$, where λ and A are strength measures for the effects of LS coupling and the crystal field, respectively.

2.1.3 Frustrated Magnetism

Contradictory interactions can sometimes inhibit a magnetic system from ordering in a conventional ground state. This refers to systems termed magnetically frustrated in which the simultaneous satisfaction of all interaction pathways is not feasible.

Magnetic frustration can be exemplified by considering the square lattice in figure 2.7a. Antiferromagnetic ordering is observed when $J_1 \gg J_2$, whereas a system is deemed frustrated when J_1 and J_2 are of comparable strengths. This either suppresses long-range ordering or results in the adoption of complex and original ground states.

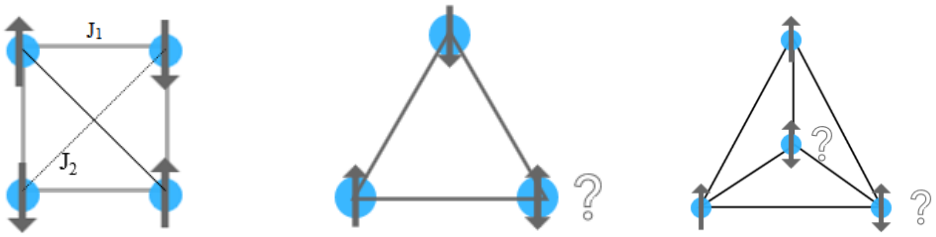

(a) Square J_1-J_2 model (b) Triangular model (c) Tetragonal model

Figure 2.7: Possible geometries demonstrating geometrical magnetic frustration for Ising spins.

Of particular interest to this study are geometrically frustrated magnets. Frustration in this case derives from the conflict between the crystallographic arrangement of magnetic moments and exchange interactions. It is important to first note that depending on the properties of the magnetic ion and its crystal environment, the direction of magnetic moments can be constrained to either one (Ising), two (XY), or three (Heisenberg) dimensions. A simple demonstration of geometrical frustration can be observed using Ising spins on a triangle as illustrated in figure 2.7b. The spatial positions of the magnetic moments does not allow for all three antiferromagnetic exchange interactions to be satisfied and thus the system does not have a particular minimum energy state. Instead, such systems are characterized by a large ground state degeneracy where there are various possible ground state configurations [4, 11]. A tetrahedron such as that in figure 2.7c is the triangular counterpart for geometrical frustration in three dimensions.

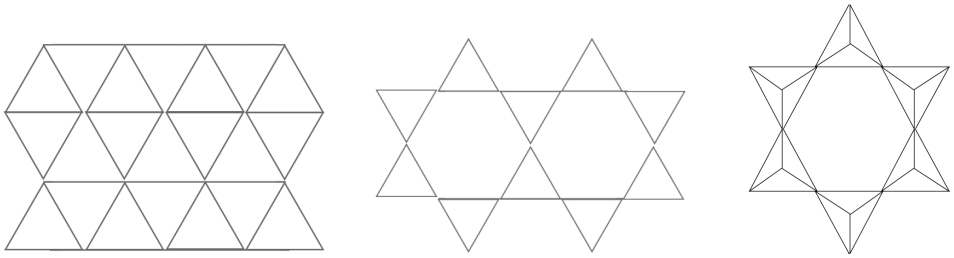

(a) Triangular (b) Kagome (c) Pyrochlore

Figure 2.8: Examples of commonly studied geometrically frustrated lattices.

Crystal systems based on the triangular plaquette are prominent in geometrical frustration studies. Edge sharing (e.g. $KTi(SO_4)_2$ [2]) and corner sharing "Kagome" (e.g. $Zn_xCu_{4-x}(OH)_6Cl_2$ [20]) triangular lattices viewed in figure 2.8a-b are examples

of two-dimensional frustrated systems, where corner sharing geometries are more strongly frustrated. In three dimensions, geometrical frustration is exemplified in corner sharing tetrahedrons forming a pyrochlore structure (e.g. $Y_2Mo_2O_7$ [21]) as viewed in figure 2.8c. This study focuses on edge sharing triangular lattices belonging to the anhydrous alum family.

2.2 Anhydrous Alums

The anhydrous alums are a family of materials characterized by the general formula $AB(XO_4)_2$, where the constituents are defined as:

$$A = A^+, A^{2+} \mid B = B^{3+}, B^{4+} \mid (XO_4) = (XO_4)^{2-}, (XO_4)^{3-} \tag{2.18}$$

Essentially, any combination of ions that can satisfy the chemical valency is applicable [2, 22–34]. While anhydrous alums can crystallize in a variety of symmetries ranging triagonal $P\bar{3}$ [22], orthorhombic Pna21 [32] and Cmca [33], and triclinic $P\bar{1}$ [34], this study is concerned with species exemplified by the C2\m monoclinic naturally occurring mineral yavapaiite ($KFe(SO_4)_2$). Structurally, yavapaiite consists of BO_6 octahedra corner-linked to XO_4 tetrahedra. Illustrated in figure 2.9a-b, such an arrangement forms a quasi two dimensional layered structure of edge-sharing anisotropic triangular $[B(XO_4)_2]^-$ sheets separated by large A cations [2].

Most important for this study are the magnetic properties exhibited by anhydrous alums with the yavapaiite archetype, first reported by S. Bramwell [22] as candidate materials for studying two-dimensional frustrated triangular lattices. Since then, a multitude of such systems have been reported to manifest exotic magnetic ground states. Examples include but are not limited to the one dimensional Heisenberg chain antiferromagnet $KTi(SO_4)_2$ [2] and two dimensional ferromagnetic $RbCr(SO_4)_2$ [24].

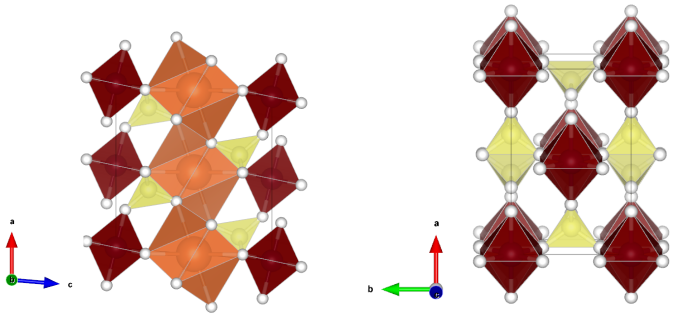

(a) (b)

Figure 2.9: (a) $AB(XO_4)_2$ projected on the a-c plane. (b) $AB(XO_4)_2$ projected on the a-b plane, where A cations are omitted for clarity in viewing the triangular sheets. BO_6 octahedra are presented in red, XO_4 tetrahedra are in yellow, and BaO_{10} bi-capped square anti-prisms are in orange. The structure was generated using the VESTA visualization software [1].

The materials studied for this thesis are $RbTi(SO_4)_2$, $CsTi(SO_4)_2$, $NaFe(SO_4)_2$, and $BaMo(PO_4)_2$. RTS and CTS are examined as to complete the series of Ti^{3+} materials [2] and investigate the difference in their properties based on the different cations. NFS follows up on the possible magnetic structure of Fe^{3+} yavapaiite materials [22]. The low temperature magnetic properties of BMP are examined for the first time.

2.3 Preparative Methods

2.3.1 Solid-state synthesis

One of the most regularly used synthetic techniques for inorganic materials is solid-state synthesis. Often called the ceramic-route, its popularity stems from being conceptually straightforward and easily applicable in both laboratories and industrially. Simply put, by combining the starting materials in their solid states, as the name suggests, the steps to follow include grinding, pelletizing, with subsequent heat treatments as illustrated in figure 2.10. Frequently, the starting materials include oxides, nitrates, and carbonates of the required elements. The first step, grinding, ensures a homogeneous mixture of uniform particle size as to aid in obtaining the desired stoichiometry. Grinding can be carried out manually using a mortar and pestle, or assisted using equipment such as a ball mill. Grinding is usually followed by pelletizing so as to maximize the contact area between the fine particles. The pellet is then transferred to a crucible and heated up in a furnace with a controlled environment for a specified amount of time. A surface reaction commences where the reactants diffuse from the bulk to the interface between the crystallites [13, 35], thus explaining the need for pelletization.

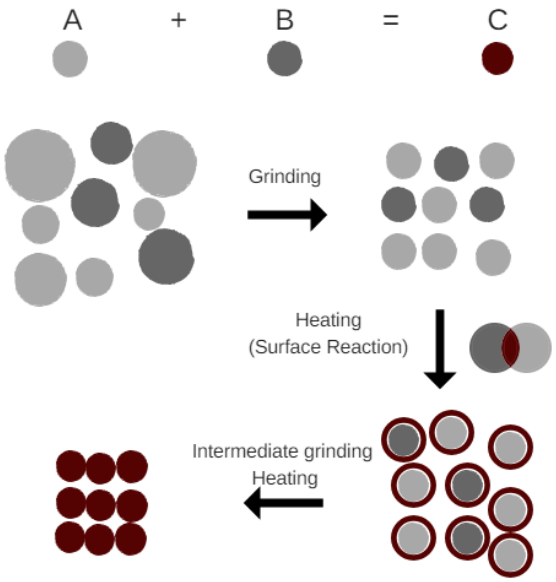

Figure 2.10: Simplified illustration of the crucial steps in solid state synthesis.

2.3.2 Solvothermal Synthesis

Another frequently used preparative technique for inorganics is solvothermal synthesis. Different procedures can fall under the header (e.g. sol-gel, spray drying), and this study adopts the following steps. A mixture of the starting materials is prepared by solvating the reactants in an appropriate solvent. The solution is stirred to ensure homogenization, and the mixture is heated to initiate the reaction and obtain the final product. Depending on the product and on the oxidation state required, the reaction can be carried out in a beaker, an autoclave, or a high pressure tube.

2.4 Characterization Techniques

2.4.1 Diffraction

Structural determination, whether crystallographic or magnetic, is most commonly performed utilizing diffraction techniques. Diffraction is based on the scattering of waves upon interacting with a grating. Adequate resolution requires that the wavelength of the incident beam is comparable in magnitude to the size of the scattering object [36]. Similar in concept to a grating, crystals are constructed from a regular repeating array. Thus, with inter-atomic distances of 1-3 Å, crystals can diffract X-rays ($\lambda = 0.1 - 10$Å) and neutrons of same wave length. A necessary condition for observing significant diffraction is constructive interference, where the scattered waves emerge in-phase with one another [13, 37]. This is eloquently stated by the Bragg equation, indicating the presence of diffraction peaks when the phases of the incident and diffracted beams are equal and a monochromatic beam is used:

$$n\lambda = 2d_{hkl}sin\theta_{hkl} \tag{2.19}$$

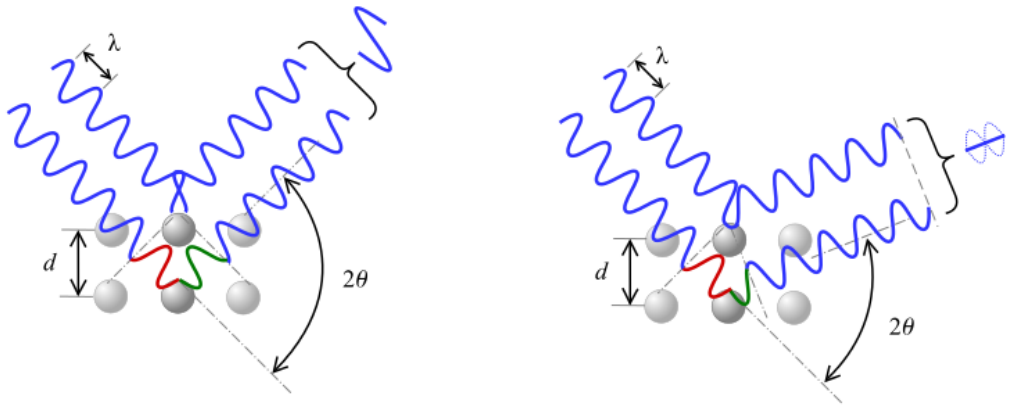

(a) Constructive interference (b) Destructive interference

Figure 2.11: Possible scattering arrangements indicating (a) constructive interference for Bragg's law and (b) destructive interference.

Here, n is an integer, d_{hkl} is the spacing between the hkl Miller crystallographic planes, and θ is the angle between an incident beam of wavelength λ and a particular crystal plane. Equation 2.16 is constructed based on the experiments of Lawrence and William Bragg in 1913 [38], following up the work completed by Max von Laue before them. Even though the Bragg equation was originally used to describe the diffraction of X-rays, it is equally applicable to neutron and electron diffraction. The physical interpretation of the Bragg equation is that it describes the conditions for constructive scattering as depicted in figure 2.11a where the wavelength of the incident and diffracted radiations are equal.

2.4.1.1 X-ray Diffraction

X-ray diffraction (XRD) is one of the the most frequently used characterization techniques in crystallography. Explaining its popularity is the ease of X-ray generation in a laboratory, thus allowing for quick qualitative phase recognition, phase purity analysis to a certain degree, and structural determination with a relatively short data acquisition time in a nondestructive manner. When an X-ray source radiates a sample, whether in a single-crystal or powder form, the electromagnetic waves are elastically diffracted by the material's electron clouds. The intensities of the diffracted radiation are collected and plotted versus 2θ, the angle between the incident and the diffracted beams, thus forming a diffractogram. Using the Bragg equation (eq. 2.16), θ can be directly related to the d-spacing d_{hkl}, which can in-turn be directly related to the lattice parameters. Further information regarding the spatial atomic positions and occupancies can be obtained based on the crystal's electron density relation at any point (x, y, z) given by [13, 37, 39]:

$$\rho(x, y, z) = \frac{1}{V} \sum_{hkl} |F_{hkl}| e^{i\alpha_{hkl}} e^{(-2\pi i hx + ky + lz)} \tag{2.20}$$

Here, V is the volume of the unit cell, (x, y, z) are atomic positions, α is the phase, and hkl are the crystallographic plane Miller indices. The Fourier transform of the electron density relation is a mathematical function known as the structure factor, given in a simplified form as [37]

$$F_{hkl} = \sum_{i} f_i e^{2\pi i (hx_i + ky_i + lz_i)} \tag{2.21}$$

where the form factor f_{i} defines the ability of the atom i, with spatial position (x, y, z), to scatter X-ray radiation, and the spatial dependence of that scattering. One can define the structure factor, and thus extract the required information, by tracing backwards from the intensity of the diffracted beams as it is directly associated with the square modulus structure factor by [37]:

$$I_{hkl} = C_{hkl} |F_{hkl}|^2 \tag{2.22}$$

C_{hkl} is a constant based on instrumental parameters, polarization corrections, and corrections for sample radiation absorption. Structural determination using XRD is often made challenging by several factors. First, diffraction based techniques

illustrate one of the limitations imposed by quantum mechanics: the inability of determining both the phase and amplitude of the structure factor. As I_{hkl} is related directly to the modulus of the structure factor, information about its phase is lost [13, 40]. Another limitation, particular to XRD, is that the scattering strength is based on the number of electrons, thus increasing as atoms get heavier, making it inherently more difficult to distinguish between isoelectronic elements and between atoms of largely varying weights.

2.4.1.2 Neutron Powder Diffraction

Neutron powder diffraction (NPD) studies are usually performed to compliment data collected using XRD. Even though conceptually similar, neutrons are commonly employed as to go beyond the limitations inherent to XRD. This is made possible by two main advantages intrinsic to neutrons, namely, charge neutrality and possessing a spin.

Scattering from nuclei rather than electron clouds is a crucial benefit offered by NPD. Unlike XRD techniques, the scattering strength of elements varies semi-randomly across the periodic table when using neutrons, allowing for one to distinguish between isotopes, isoelectronic elements, and species in crystals comprised of both light and heavy elements. The form factor also remains constant regardless of 2θ, allowing for consistent intensities throughout a diffractogram [36]. An additional advantage in structural determination is the ability to correctly identify bond lengths, usually altered by electron clouds in XRD studies [13].

One of the main applications of neutron diffraction is magnetic structural determination. Neutrons are excellent probes for magnetic properties as they posses a spin and therefore can scatter upon interacting with atomic magnetic moments through dipolar interactions. Thus, when a magnetic material transitions into an ordered state, additional magnetic Bragg peaks are observed. Resolving the magnetic structure and identifying its symmetry can then be completed through several analysis techniques, some of which are eloquently introduced by Rodríguez-Carvajal [41] and Ressouche [14]. Magnetic structural determination using the Rietveld method [42] will be discussed in later sections.

2.4.2 Magnetic Excitations

2.4.2.1 Spin-wave theory

In an ordered sate, magnetic excitations are termed spin waves and can be viewed as an interruption of the preferred magnetization direction. One can picture this as if a spin has been canted out of its preferred magnetization direction, thus affecting nearby spins and resulting in a cooperative propagating wave like precession of spins as illustrated in figure 2.12. Just as lattice vibrations in a solid are quantized into phonons, spin waves are quantized into spin 1 quasiparticles termed magnons [43].

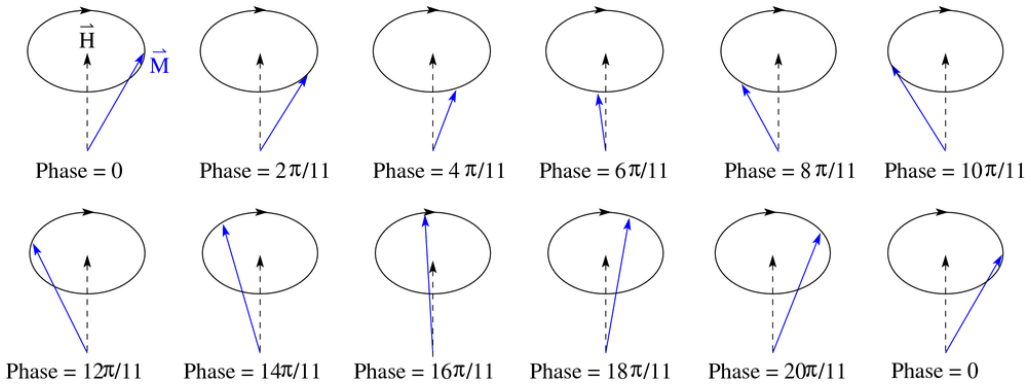

Figure 2.12: Illustration of a dispersion where spins precess about the magnetization axis. Because spin waves are periodic, they also produce a periodic spectrum in reciprocal space. This is referred to as the spin wave dispersion (example figure), whose shape and bandwidth depends on the parameters in the spin Hamiltonian. Quantifying the experimentally measured spin wave dispersion thus allows for one to probe the interactions of the system. This can be done by solving the spin Hamiltnonian.

Quantifying spinwaves allows for one to probe interactions of a system. This can be derived by solving the spin Hamiltonian using classical or quantum considerations where for the latter, a spin is flipped and propagated by using creation and annihilation bosonic (spin 1) operators [44]. As this is beyond the scope of this study, the interested reader is referred to Toth [44] or Rössler [45] for the full derivations. By solving the spin Hamiltonian, one can calculate the excitation spectrum of a system and intensities using an excitation dispersion relation, which was carried out using the MATLAB SpinW library [44] for this thesis.

2.4.2.2 Inelastic Neutron Scattering

The energy of the produced neutrons can be controlled as to coincide with the energy scale of dynamic excitations. As such, neutrons can be used to probe, among others, phonon and magnon energies [11].

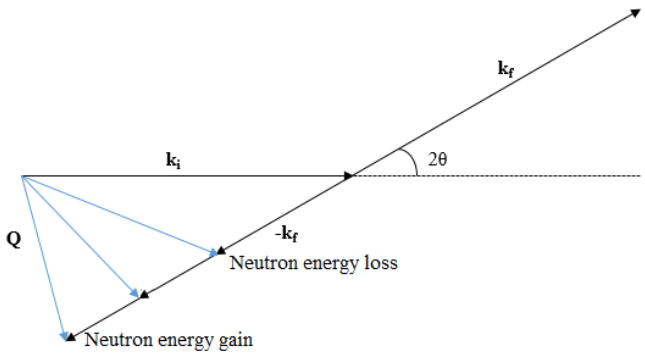

Figure 2.13: Illustration of an inelastic scattering event where initial and final neutron wave vectors are unequal.

This can be carried out using Inelastic Neutron Scattering (INS) in which the momenta of incident neutrons varies upon interacting with matter. For a neutron described by its wave vector $\mathbf{k}$ in its initial i and final (scattered) f states, this process can be represented in terms of momentum conservation expressed in the scattering vector $\mathbf{Q}$ (fig 2.13) and energy conservation such that [46]:

$$\mathbf{Q} = \mathbf{k}_i - \mathbf{k}_f \tag{2.23}$$

$$\hbar\omega = E_i - E_f = \frac{\hbar^2}{2m_n}(\mathbf{k}_i^2 - \mathbf{k}_f^2) \tag{2.24}$$

where E is energy, ω is the angular frequency, and m_n is the mass of a neutron. In order to describe the energy of the system for a known $\mathbf{k}_i$ or $\mathbf{k}_f$, INS involves measuring $\mathbf{Q}$ and ω, yielding the dynamic structure factor $S(\mathbf{Q}, \omega)$ [46].

2.4.3 Magnetometry

The determination of magnetic susceptibility is a cornerstone in magnetic characterization. Owing to its exceptional sensitivity, this study uses a DC-SQUID magnetometer for all susceptibility measurements as the studied materials are expected to have small moments. The working principle of SQUID magnetometry heavily relies on the theory of superconducting materials which can be visited in Weinstock [47] and Clarke [48] from which the following discussion is inspired. The sample is introduced into the apparatus and is surrounded by superconducting detection coils followed by submersion into a cryostat. The sample is then exposed to a magnetic field produced by a superconducting electromagnet. To convert the changes in magnetic flux into a measurable current, Faraday's law of induction is utilized by systematically varying the sample's spatial position.

The detection coils are directly linked to a DC-SQUID, a device comprised of a superconducting annulus with two Josephson junctions as illustrated in figure 2.14. Measuring the magnetization of the sample mainly depends on three properties intrinsic to superconducting materials. First, the Meissner effect indicates that unlike other materials, electromagnetic waves cannot penetrate a superconducting material at a temperature below its transition temperature. This can be explained by the formation of screening currents on the surface of the superconductor that result in magnetic fields opposing those applied [49]. An additional crucial property to consider is of quantum mechanical nature, where upon forming a Josephson junction by separating two superconductors with an insulating link of specified dimensions, a super-current, one that requires no potential difference, is tunneled through the link [49]. This is termed the Josephson effect, occurring as a result of a phase gradient between the superconducting materials. Finally, when passing through a superconducting loop, magnetic flux is quantized into fluxons defined as $\Phi_o = 2.07 \times 10^{-15} Wb$ [10]. Combining this, the current produced by moving the sample will act as a bias to the DC-SQUID, changing both its screening and critical currents in a periodic manner. This results in the formation of a measureable voltage gradient according to flux quantization. The voltage formed is proportional to the sample

induced current from which magnetization and thus the susceptibility can be inferred [37].

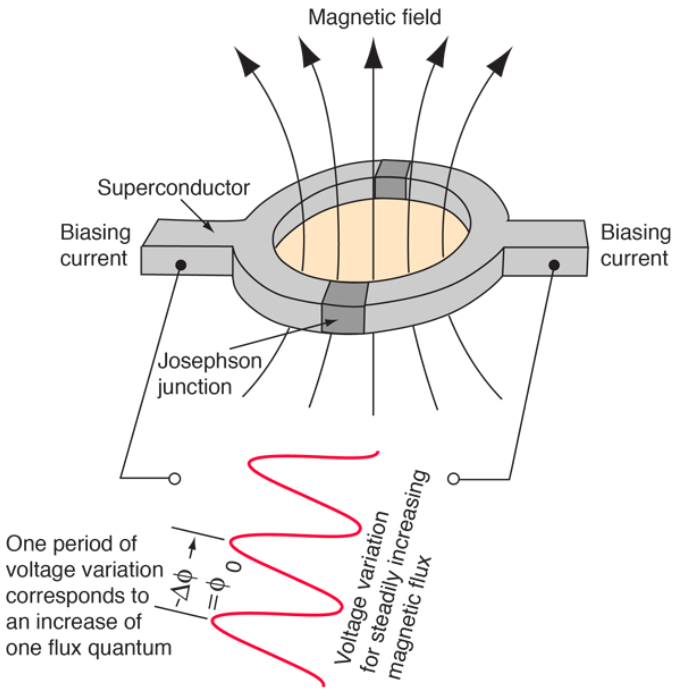

Figure 2.14: Principle components of a SQUID magnetometer. Picture obtained from [50].

2.4.4 Specific heat

Thermodynamic measurements, such as that of heat capacity, are frequently employed for the characterization of low-temperature magnetic behavior. Isobaric heat capacity is defined as the change in energy, defined as heat (Q), induced by a temperature gradient such that [51]:

$$C_p = \left(\frac{\delta Q}{\delta T}\right)_{\mathrm{p}} \tag{2.25}$$

Obtaining the specific heat is then a trivial task of accounting for the mass of the sample. The importance of this technique lies in the breadth of lattice information interpretable from its measurements as it probes thermally-triggered transitions and excitations (e.g. phonons, magnons) [51]. Thus, one can potentially identify a transition and its type from its characteristic behavior in a heat capacity versus temperature curve. For example, in a second order transition, symmetry breaking involves a change in internal energy and can be identified by a λ shaped anomaly in the specific heat curve, therefore characterizing the ordering temperature of the transition [52].

The total heat capacity of a system is comprised of multiple components. Lattice, magnetic, and electronic contributions must all be considered [53], where the importance of each component varies depending on the temperature range. In order

to precisely determine the magnetic contribution to the specific heat at low temperatures, the lattice contribution, mainly that of phonons, must be subtracted from the collected data. This can be done in different ways, as for example [51], by using the Debye T^3 approximation for insulating materials, the Einstein model, or by substracting the phonon contribution of an identical but diamagnetic counterpart of the material of interest.

While many techniques exist for measuring the heat capacity of a substance, this study uses thermal relaxation. Simply put, relaxation calorimetry is a cyclic process involving heating a sample at constant heating power to T_1 followed by a temperature decay to T_2 upon shutting off the heating power after a time t [53]. The specific heat is then fitted to a two-tau model of the relaxation such that [53]:

$$T_1(t) - T_2 = \Delta T = A_1 e^{\frac{-t}{\tau_1}} + A_2 e^{\frac{-t}{\tau_2}} \tag{2.26}$$

$$C_{sample} = K\left(\frac{A_1\tau_1 + A_2\tau_2}{A_1 + A_2}\right) \tag{2.27}$$

Where A_i is a measurable constant dependent on the heating power, K is a calculable constant, and τ_i is a time constant. In equation 2.24, the $i = 1, 2$ refer to the sample holder and the sample.

2.5 Analytical Techniques

2.5.1 Rietveld Method

The Rietveld method is a cornerstone analytical tool used in aiding both crystal and magnetic structural determination from diffraction data. Originally proposed for neutron diffraction data [42], and now equally applicable to high-quality X-ray data, the main concept of the Rietveld method is to minimize the weighted sum of squared deviations between collected and calculated diffraction patterns using least squares fitting [13]. A diffraction profile can be calculated by considering all the appropriate crystallographic (e.g. symmetry, lattice constants, atomic positions, thermal displacement factors), instrumental (e.g. zero-shift, peak shape, background), and sample based (e.g. absorption, preferred orientation) parameters [37]. Specific parameters are then chosen to be refined through minimizing the intensity weighted (w_i) sum of the squared difference between each observed ($y_{i(obs)}$) and calculated ($y_{i(calc)}$) intensity data point i using:

$$L = \sum_{i=1}^{N} w_i (y_{i(obs)} - y_{i(calc)})^2 \tag{2.28}$$

Rietveld refinement is an iterative technique, and stopping the process is heavily dependent on when the user considers the accuracy to be sufficient. Nonetheless, several statistical factors can be taken into consideration to assess the goodness of the fit. For example, three of the most frequently considered factors are the

weighted-profile R-value, its maximum value the expected R-factor [54], and the χ^2 statistic which can be defined as [55]:

$$R_{wp} = \sqrt{\frac{\sum_i w_i (y_{i(obs)} - y_{i(calc)})^2}{\sum_i w_i y_{i(obs)}^2}} \tag{2.29}$$

$$R_e = \sqrt{\frac{N}{\sum_i w_i y_{i(obs)}^2}} \tag{2.30}$$

$$\chi^2 = \left(\frac{R_{wp}}{R_e}\right)^2 \tag{2.31}$$

Where N is the number of degrees of freedom. By considering the statistical factors, a relatively small R_{wp} close to R_e and a χ^2 statistic close to unity are indicative of a good fit [54].

An essential concept to consider is that a diffraction profile must be calculated based on a suggested crystallographic model. Hence, the Rietveld method is not used for resolving a structure, but instead to determine a best fit model for the available data. For the purpose of this study, Rietveld refinement has been preformed using both TOPAS [56] and FullProf Suite [57].

2.5.2 Profile Fitting

Another structural analysis approach using diffraction data is full pattern decomposition. In this context, the two most commonly used techniques are the Le Bail [58] and Pawley [59] methods, and the former is used in this study. What separates Rietveld refinement and Le Bail fitting is how the intensities are defined. One requires no prior knowledge of structural data, but only the symmetry and unit-cell parameters for Le Bail fitting. In application, this means that the Bragg intensities are not confined to a model, but are instead partitioned and calculated based on the observed intensities. The observed intensities ($I_{k(obs)}$) can be calculated in a similar manner to the Rietveld method by separating the contribution of different k Bragg reflections as a function of the calculated intensity ($I_{k(calc)}$) such that [60]:

$$I_{k(obs)} = \sum_i \frac{(y_{i(obs)} - y_{i(bkg)}) w_{ik} I_{k(calc)}}{\sum_k w_{ik} I_{k(calc)} - y_{i(bkg)}} \tag{2.32}$$

Here, $y_{i(obs)}$ and $y_{i(bkg)}$ are the collected data points and their respective backgrounds and w_{ik} is a calculable variable based on factors such as the peak profile and zero shift. Initially, the calculated intensities are given a constant value which is varied upon fitting a chosen set of parameters using least squares minimization [61]. Le Bail fitting is usually implemented as a complementary technique to extract a set of initial parameters for later refinement, test initial symmetry guesses, or as means to account for an extra phase alongside a Rietveld refinement. In this thesis, Le Bail fitting was completed using FullProf Suite [57].

3

Methods

3.1 Material Preparation

3.1.1 $BaMo(PO_4)_2$

Solid-state synthesis was chosen as the synthetic route for BMP. First, a stoichiometric mixture of $BaCO_3$ (Alfa Aeser 99.9%), MoO_2 (Alfa Aesar 99.0%), and $(NH_4)_2HPO_4$ (Alfa Aesar 98+%) is ground in an agate mortar and pestle for an adequate amount of time according to the reaction:

$$BaCO_3 + MoO_2 + 2\,(NH_4)HPO_4 \longrightarrow BaMo(PO_4)_2 + CO_2 + 3\,H_2O + 4\,NH_3 \quad (3.1)$$

An initial heat treatment at 600°C/12h was performed to eliminate water, ammonia, and carbon dioxide. The mixture was submitted to further heat treatments with intermediate grinding and pelletizing, followed by a final heating stage at 1000°C/72h. The reaction was carried out under high vacuum, and several attempts at using an argon inert environment were also successful. It should be noted that larger masses require longer heating periods and that an alumina crucible was used.

3.1.2 $ATi(SO_4)2$

The synthesis of $ATi(SO_4)_2$ (A=Rb, Cs) compounds adopts the procedure specified by Nilsen [2]. A_2SO_4 (Alfa Aesar 99.9%), $Ti_2(SO_4)_3$ (Alfa Aesar 20% in 1-4% sulfuric acid), and H_2SO_4 are combined in an autoclave with a molar ratio 2:7:15. The reaction proceeds at 155°C for 48h or 60h for Cs and Rb, respectively, followed by a cooling period of 24h. To reduce the amounts of formed impurity phases, the retrieved product is then washed using acetone. It should be noted that the presented conditions are found to give the highest crystallinity, as the molar ratios, reaction temperatures, and reaction times were optimized by systematically varying the reaction conditions.

3.2 Instrumentation

3.2.1 Powder X-ray Diffraction

In this study, all XRD measurements were completed using a laboratory Bruker D8 Advance© X-ray powder diffractometer at room temperature. An X-ray tube generates radiation using a Cu anode in combination with a germanium (111) monochromator, resulting in monochromatic CuK_α ($\lambda = 1.541$Å) X-rays. A silicon based sample holder is used. Data acquisition is viewed in real-time using DIFFRAC.SUITE. Phase recognition and pattern matching is performed using the Bruker EVA© software in combination with an ICDD (International Center for Diffraction Data) database.

3.2.2 Neutron Powder Diffraction

All neutron powder diffraction data used for this thesis were collected at the ISIS Neutron and Muon Source, Rutherford Appleton Laboratory, Didcot, UK. This facility uses a spallation source, where a tungsten target is bombarded by clusters of protons accelerated in a synchrotron ring to speeds comparable to the speed of light. Atomic nuclei and neutrons spall from the target upon collision, which is followed by directing the neutrons into a moderator as they make their way towards the specific instrument. Based on the application of the instrument, different moderators such as water, heavy water, solid methane, or liquid hydrogen can be used to obtain the appropriate distribution of neutron de Broglie wavelengths. The bunched nature of the protons results in a pulsed neutron source. Frequently, the whole beam, with variable wave-length neutrons, is then directed towards the sample of interest to avoid losing intensity. A monochromator is thus deemed unnecessary, and the time-of-flight (TOF) of the neutrons is detected versus the intensity and related to the Bragg equation as:

$$\lambda = \frac{h}{p} = \frac{h}{mv} = \frac{ht}{mD} \tag{3.2}$$

$$\frac{ht}{mD} = 2d_{hkl}sin\theta \tag{3.3}$$

Here, h is Planck's constant, m is the neutron mass, D is the distance between the source and the detector, and finally t is the neutron time of flight.

Nuclear and magnetic structural analysis of BMP were completed through Rietveld refinement of neutron diffraction data collected at the ISIS Neutron and Muon facility. Both the High Resolution Powder Diffractometer (HRPD) [62] and the long wavelength diffractometer WISH [63] were used. Experimental conditions are summarized in table 3.1. Data compilation and reduction was completed using the Mantid Project [64].

Instrument	d-spacing range [Å]	Detection Banks	Sample Mass [g]	Temperatures [K]
HRPD	0.80 - 15.7	3	5.00	300. - 2.00
WISH	0.70 - 50.0	5 Pairs	10.0	30.0 - 2.00

Table 3.1: Experimental conditions on HRPD and WISH for BMP.

3.2.3 Inelastic Neutron Scattering

The excitation spectrum of $BaMo(PO_4)_2$ was measured using the MERLIN spectrometer at ISIS [65]. MERLIN is a direct geometry (fixed $\mathbf{k}_i$) TOF spectrometer. The variable wave-length pulsed beam is first allowed into a chopper system as to specify the energy scale of the incident neutrons. Neutrons of undesirable energies are absorbed by the material comprising the choppers and a beam of specified energy is formed upon passing an opening in the rotating choppers such that only neutrons of the correct speed i.e. energy are able to pass. The distance from the sample and $t = 0$ for the TOF measurement begin at the choppers. The formed beam scatters of the sample with known initial conditions, and the scattering angle 2θ, vertical angle γ, and the time required for the scattered beam to reach an array of detectors are measured. From this, the final neutron energy E_f is determined and the scattering vector $\mathbf{Q}$ is finally obtained. The experimental conditions for the study of BMP are given in table 3.2. Data reduction and analysis was carried out using the Mantid Project [64]. Modelling of the resulting excitation dispersion relation was carried out using the SpinW library [44].

Energy [meV]	Sample Mass [g]
50.0, 19.0, 10.0	15.0
Temperature [K]	**Exposure Time [min]**
4.00	120.
10.0	120.
20.0	120.
40.0	120.
60.0	45.0
100.	20.0

Table 3.2: Experimental conditions for BMP on MERLIN.

3.2.4 Magnetometry

All susceptibility measurements were carried out using a Quantum Design Magnetic Property Measurement System (MPMS)© utilizing a SQUID magnetometer. Milligram powder samples were inserted in a plastic capsule alongside teflon to maintain the sample in place. The capsule was then introduced into a straw-like plastic container and inserted in the MPMS system. DC susceptibility measurements were then carried out using both zero-field (ZFC) and field cooling (FC) protocols. For the former, samples were cooled down to base temperature with no applied field, followed up by heating and measurements in a 1000 Oe applied field, while for the latter, the samples were cooled in the applied field.

3.2.5 Specfic Heat

To carry out specific heat measurements, packed thin samples were first prepared by pelletization. Samples were then mounted on a puck platform by using a thermal grease to ensure thermal contact. The platform is suspended by thin conducting wires and is connected to multiple thermocouples. In order to ensure an accurate measurement, the puck is inserted into a depressurized vessel to avoid thermal losses with gases. A Quantum Design PPMS© was used which follows a relaxation calorimetry technique similar to that described in section 2.4.4.

4

Results & Discussion

4.1 $BaMo(PO_4)_2$

4.1.1 Nuclear Structure

The determination of $BaMo(PO_4)_2$ crystal structure was carried out using multiple techniques. Initial samples were tested using laboratory powder XRD following the method outlined in section 3.2.1. Using FullProf Suite [57], the presence of the sought C2/m monoclinic phase was established through Rietveld refinement (figure 4.1). The unit cell parameters obtained through the refinement did not deviate from the published single crystal structure [66] and are presented in table 4.1.

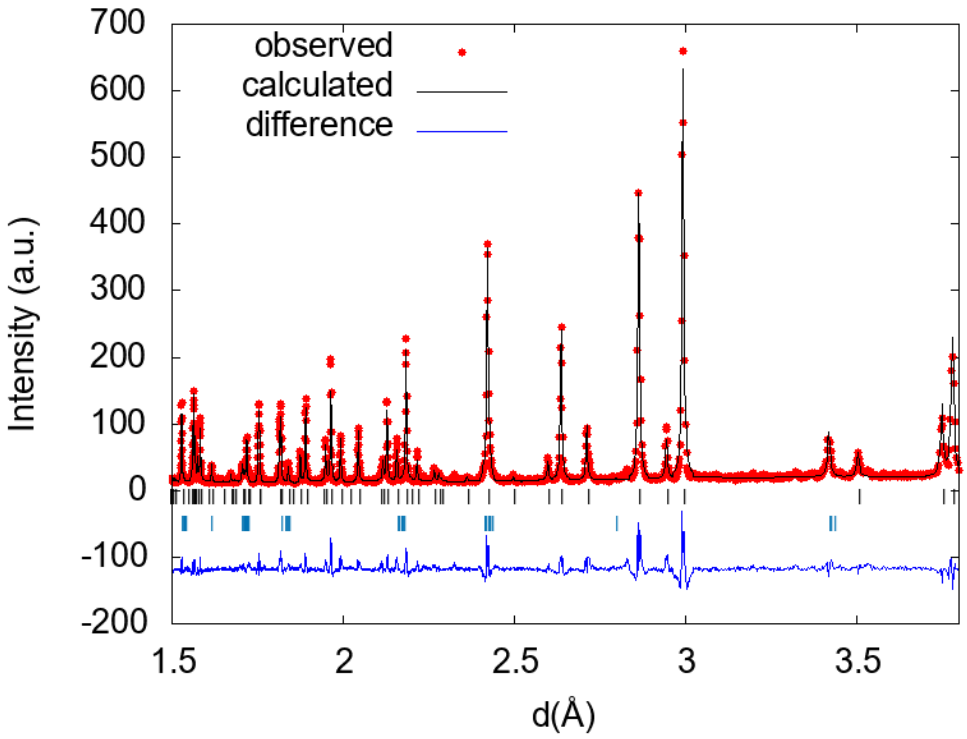

Figure 4.1: Rietveld refinement of $BaMo(PO_4)_2$ using XRPD data.

Impurity phases were noted and the major excess phase was determined as MoO_2. Pattern matching indicates the possible presence of minor $Ba_2P_2O_7$ tetragonal and hexagonal phases which were difficult to include in the refinement model. The presence of impurity phases possibly indicates that further heat treatments are required to complete the reaction. This was limited by the laboratory equipment present as the available vacuum furnace does not allow for temperatures surpassing 1273 K.

Table 4.1: Unit cell parameters for BMP obtained form powder XRD Rietveld refinement.

a [Å]	8.2061(1)
b [Å]	5.2735(1)
c [Å]	7.8212(3)
β [°]	94.7198(1)

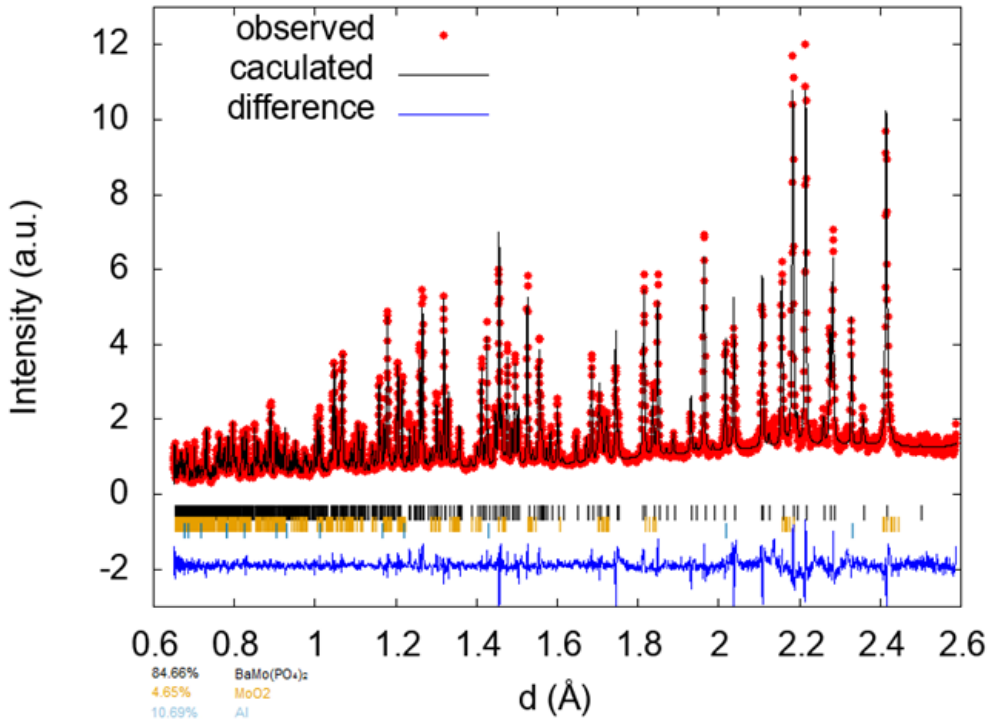

Figure 4.2: $BaMo(PO_4)_2$ NPD Rietveld refinement at 2 K.

Further nuclear structural determination was carried out using the HRPD diffractometer at ISIS. The main purpose of this diffraction study was to probe the magnetic structure of BMP, and thus the sample was investigated at a temperature of 2 K and 50 K, above the transition to allow for the isolation of weak signals by temperature subtraction. Refining the C2/m model to the high resolution data provided an excellent fit and the crystallographic data are reported in tables 4.2 and 4.3. Because small d-space regions contain a breadth of nuclear information, the refinement model weighted the smallest d-spacing detection banks the highest. The

refined structure is presented in figure 4.3. No magnetic peaks were conclusively observed, even in the temperature subtracted data. Discrepancies between PXRD [66] and NRPD data may mainly be explained by the variation of the measurement temperature.

Table 4.2: BMP refined unit cell parameters on HRPD at 1.5K. R_p=2.31.

a [Å]	8.1760(1)
b [Å]	5.2760(1)
c [Å]	7.8005(1)
β [°]	94.8481(6)

Table 4.3: Refined crystallographic information for BMP on HRPD at 2 K.

Atom	Site	x	y	z	Occ	B_{iso}
Ba	2a	0.0000	0.0000	0.0000	1.00	0.43(2)
Mo	2c	0.0000	0.0000	0.5000	1.00	0.09(1)
P	4i	0.1291(2)	0.5000	0.2912(2)	1.00	0.25(1)
O	8j	0.0227(1)	0.2611(1)	0.3114(1)	1.00	0.50(1)
O	4i	0.2648(1)	0.5000	0.4403(1)	1.00	0.34(2)
O	4i	0.1875(1)	0.5000	0.1119(1)	1.00	0.29(1)

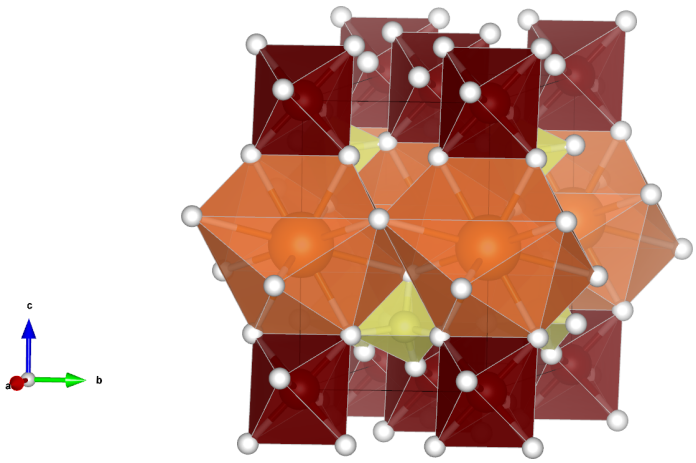

Figure 4.3: The crystal structure of $BaMo(PO_4)_2$ as viewed along the <100> plane visualized using VESTA [1] where Mo^{4+} is red, Ba^{2+} is orange, P^{8+} is in yellow, and O^{2-} is in white.

Additional structural refinement was performed on data collected at 30 K on the WISH instrument at ISIS (fig 4.4). This refinement was carried out to obtain structural and instrumental parameters to be used as the starting model for the low temperature magnetic refinement that follows. An approximately 10 g sample comprised of ten 1 g samples was used. The resulting unit cell parameters and crystallographic information are presented in tables 4.4 and 4.5, respectively.

Table 4.4: BMP refined unit cell parameters on WISH at 30 K. R_p=2.87.

a [Å]	8.1805(4)
b [Å]	5.2785(1)
c [Å]	7.8037(8)
β [°]	94.8368(3)

Table 4.5: Refined crystallographic information for BMP on WISH at 30 K.

Atom	Site	x	y	z	Occ	B_{iso}
Ba	2a	0.0000	0.0000	0.0000	1.00	0.42(9)
Mo	2c	0.0000	0.0000	0.5000	1.00	0.26(1)
P	4i	0.1300(9)	0.5000	0.7928(1)	1.00	0.48(7)
O	8j	0.0219(4)	0.2610(1)	0.8109(3)	1.00	0.92(2)
O	4i	0.2665(1)	0.5000	0.9406(5)	1.00	0.74(3)
O	4i	0.1860(9)	0.5000	0.6122(6)	1.00	0.91(2)

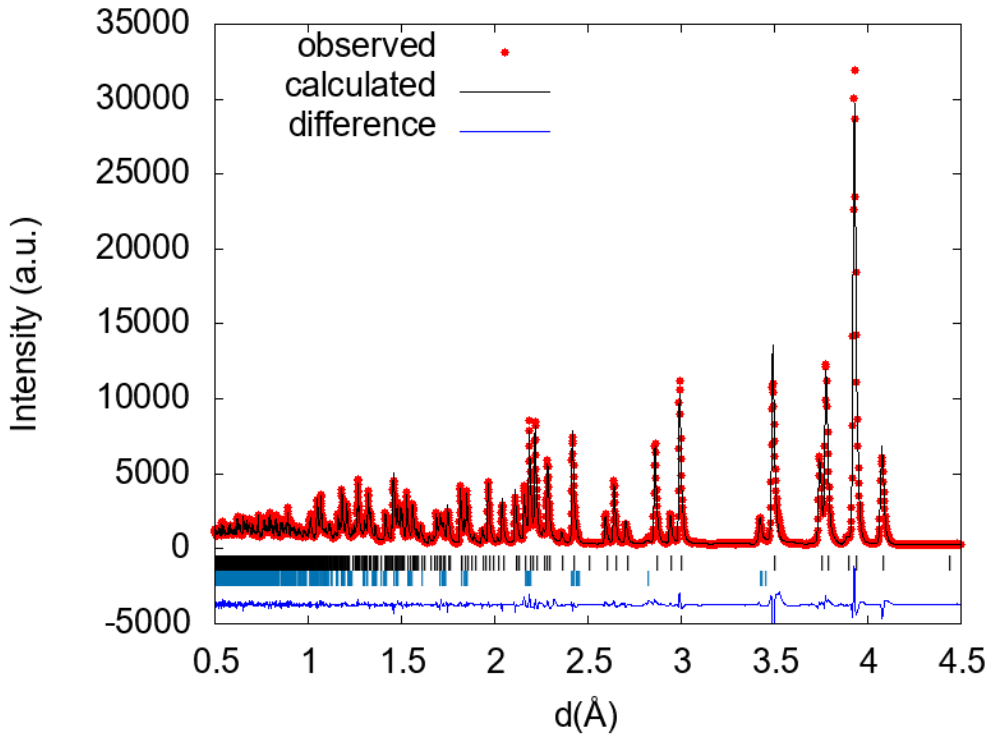

Figure 4.4: Rietveld refinement of $BaMo(PO_4)_2$ WISH NPD data at 30 K.

4.1.2 Magnetic Structure

4.1.2.1 Physical Properties

The temperature dependence of BMP's magnetic susceptibility was investigated using DC ZFC measurements under an applied field of 1000 Oe and is shown in figure 4.5. At high temperatures ranging 140 K - 300 K, the susceptibility follows the Curie-Weiss model expressed as:

$$\chi_n = \frac{C}{T_N - \theta_w} + \chi_0 \tag{4.1}$$

Other than the Curie C and Weiss θ_w constants seen in equation 2.12, an additional χ_0 term is included to account for the background, the core-shell electron diamagnetic contribution, Van Vleck paramagnetism, and the contribution of impurity phases (e.g. MoO_2). Fitting parameters are presented in table 4.6.

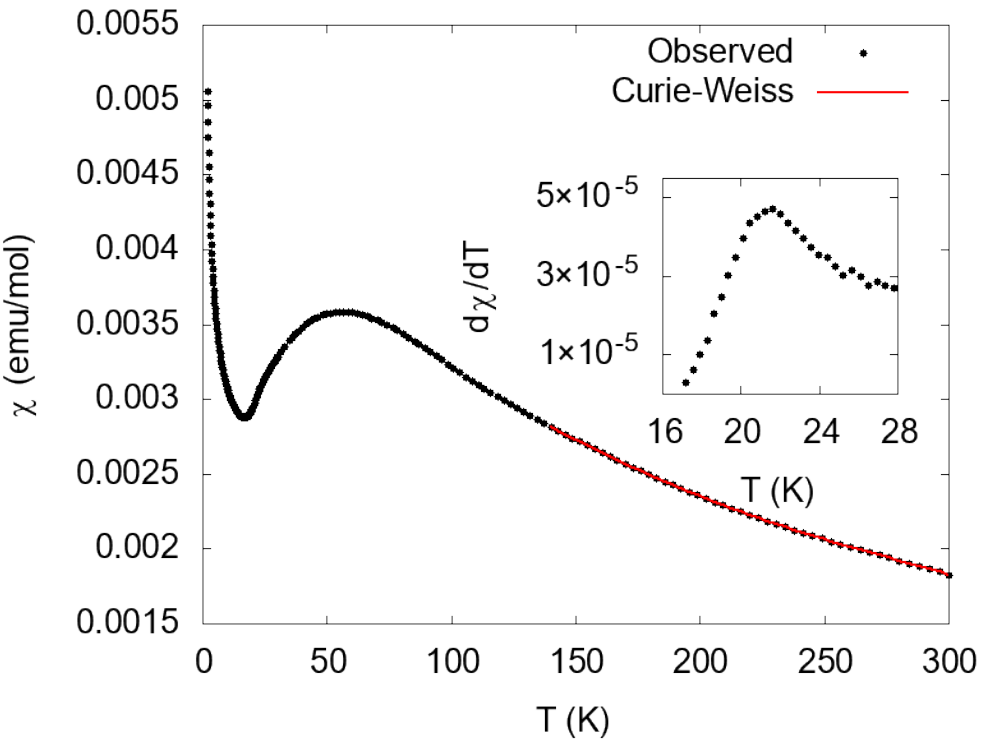

Figure 4.5: Black circles: DC molar magnetic susceptibility as a function of temperature measured in 1000 Oe applied magnetic field. Red line: Curie-Weiss model fit according to equation 4.1. Inset: Temperature derivative of the magnetic susceptibility as a function of temperature, magnified to the range of expected long-range ordering transition.

Using the parameters fitted in the CW model, several physical properties can be inferred. In comparison to the spin-only $\mu_{eff} = 2.83\mu_B$ value for Mo^{4+}, the fitted effective moment is $2.71(2)\mu_B$. This suggests that the orbital contribution may not

Table 4.6: Resulting parameters for the Curie-Weiss law fit.

C [K emu mol^{-1}]	0.919(7)
θ_w [K]	-175.(1)
χ_0 [emu mol^{-1}]	1.02(3)$\times 10^{-4}$
μ_{eff} [μ_B]	2.71(2)

be entirely quenched. It is also noted that the background parameter χ_0 is positive. Potentially, this could be explained by the positive paramagnetic contribution of the impurity MoO_2 phase [67] and/or Van Vleck paramagnetism.

A negative Weiss constant of $\theta_w = -175.0\ K$ indicative of antiferromagnetic interactions is observed. Onset of long range ordering is apparent at T_N=21 K. This can be seen at either the inflection point in the susceptibility curve or at the maximum of $d\chi/dT$. Absolute Weiss constants much greater than the ordering temperature can also imply magnetic frustration if one defines a frustration coefficient f as:

$$f = \frac{|\theta_w|}{T_N} \tag{4.2}$$

Geometrical frustration is thus expected for BMP as $f \approx 8$, where $f \geq 10$ indicates strong magnetic frustration or low dimensionality [4].

Deviations from the Curie-Weiss law are seen at low temperatures. Short range interactions characterized by broad features in the susceptibility curve are identified around 70 K. A sharp increase in susceptibility at temperatures below 10 K is attributed to the contribution of the paramagnetic impurity phases.

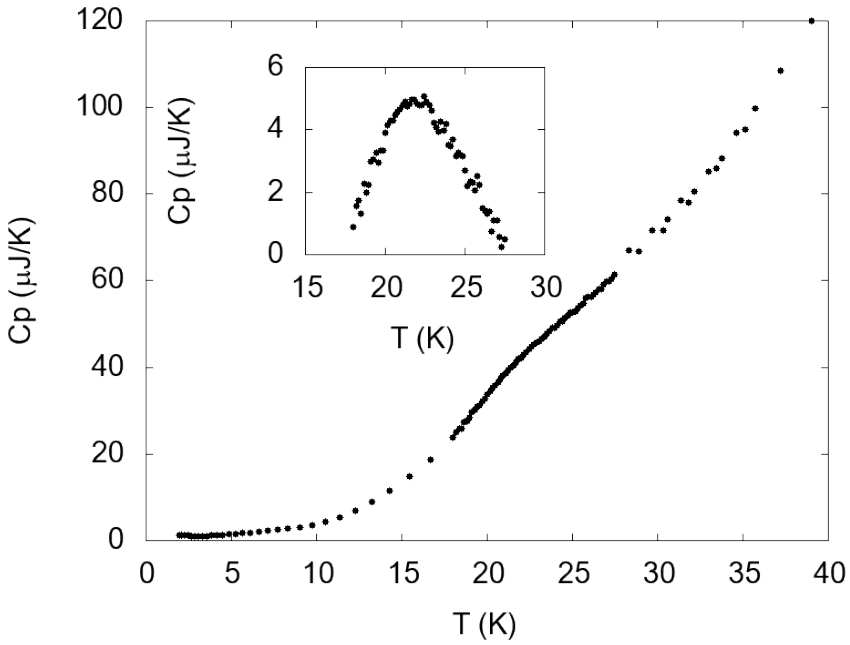

Figure 4.6: The specific heat of $BaMo(PO_4)_2$ as a function of temperature. Inset: Temperature dependence of the phonon contribution subtracted specific heat.

The zero-field specific heat data does not show an easily visible sharp lambda anomaly characteristic of long range ordering. However, upon subtracting the lattice contribution from the specific heat data as seen in the inset of figure 4.6, a clear transition is seen around 21 K, similar to the transition observed in the susceptibility curve. The subtraction was carried out using the following empirical expression:

$$C_p = x_1 T^3 + x_2 T^5 + x_3 T^7 \tag{4.3}$$

4.1.3 Neutron Diffraction

To investigate the long-range magnetic ordering of BMP, low temperature NPD data was collected below the transition temperature at 2.5 K on the WISH diffractometer. Well defined magnetic Bragg peaks are observed, as seen in figure 4.7, and indexed using K-search [57]. A commensurate ordering propagation vector of $\kappa = (\frac{1}{2}, \frac{1}{2}, \frac{1}{2})$ was identified, indicating a magnetic supercell twice the size of the nuclear unit cell. Representational analysis was carried out using BasIreps [57] and MAXMAGN [68] was used to determine the most probable allowed magnetic space groups . The resulting group was identified as $P_s\bar{1}$ and applied in modelling the magnetic structure using Rietveld refinement. All structural and instrumental parameters were fixed to their nuclear structure refinement values, and only the magnetic moment was refined. The resulting magnetic structure can be seen in figure 4.7. An ordered

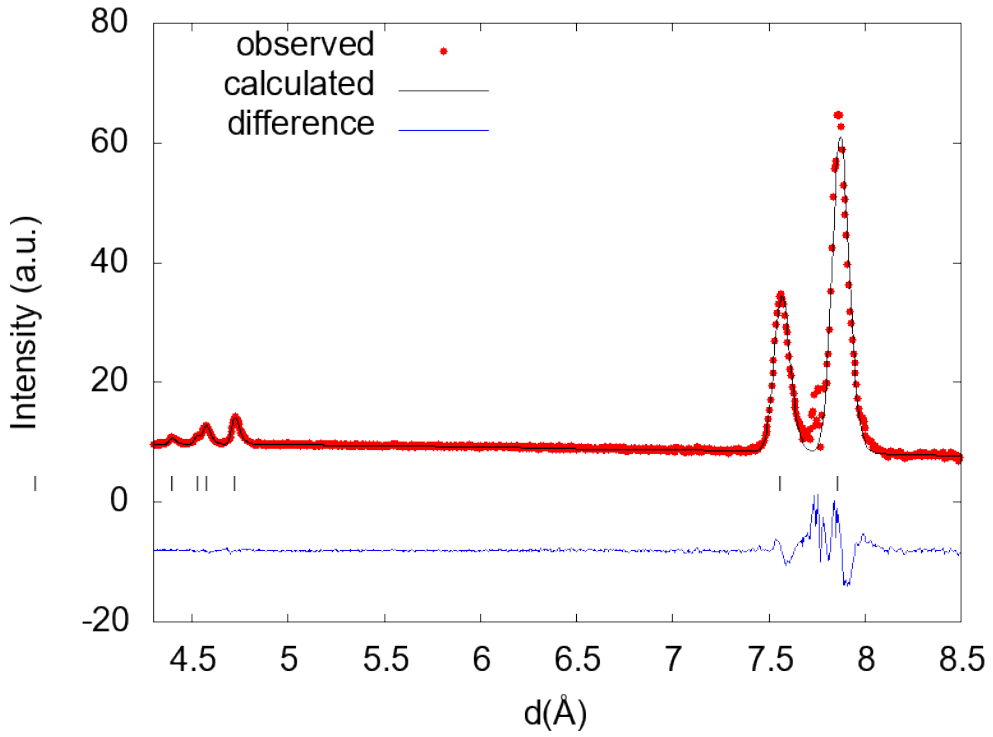

Figure 4.7: Rietveld refinement of $BaMo(PO_4)_2$ WISH NPD data with R=11.85. The diffractogram is a result of subtracting low (2.5 K) from high (30 K) temperature data.

state with antiferromagnetic nearest-neighbour (NN) interactions and ferromagnetic interactions along the <110> direction is observed. This behavior is indicative of competing interactions, as to be expected from a geometrically frustrated system. In comparison to the spin-only effective moment $2.83\mu_B$ of Mo^{4+}, a value of 1.22(1) μ_B results from the refinement. This reduction is a signature of strong-spin orbit coupling, and in combination with the collinear structure, single-ion anisotropy is suggested. As a result of the long distances between Mo^{4+} cations, superexchange interactions with the shortest Mo-P-O-P-Mo paths are expected to dominate. Thus, interactions along the b-axis (J) and the <110> direction (J'), defined in figure 4.8b, are likely to be the most prominent as is the case with similar systems [2].

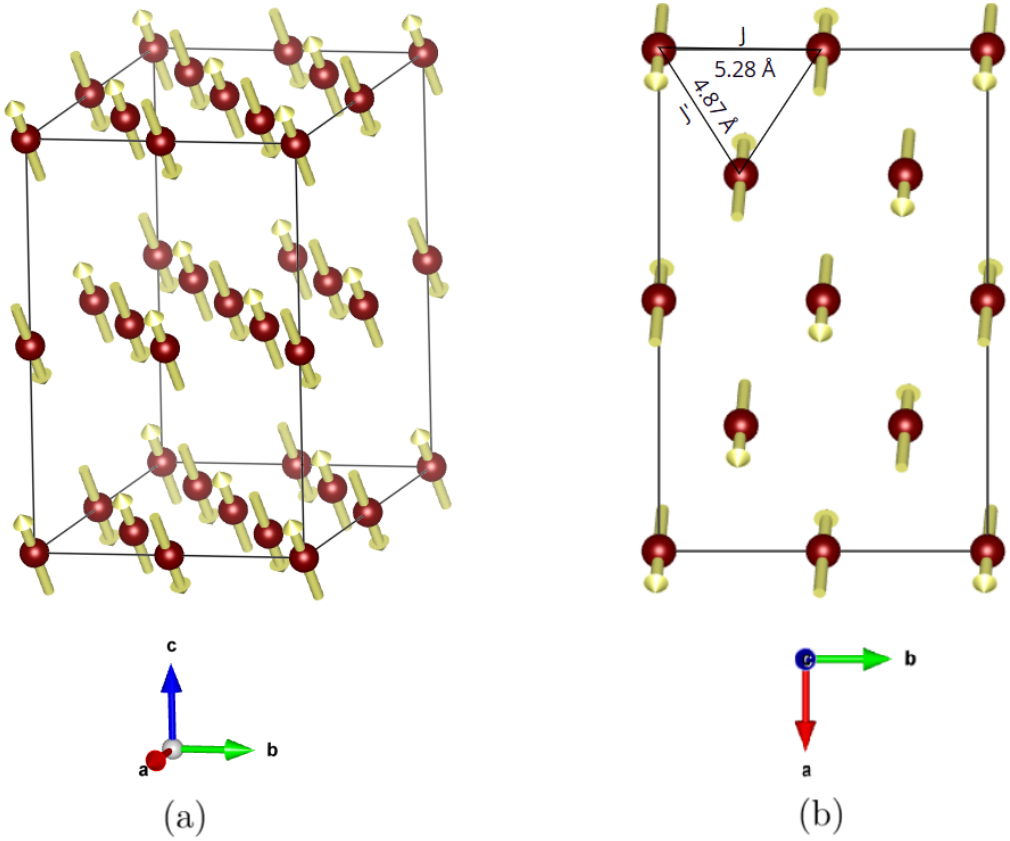

Figure 4.8: (a) The suggested magnetic structure of $BaMo(PO_4)_2$ determined from low temperature NPD structural refinement. (b) The magnetic structure viewed along the c*-axis with exchange interactions J and J' defined along the b-axis and the <110> directions, respectively.

4.1.4 Neutron Spectroscopy

The magnetic excitation spectrum of $BaMo(PO_4)_2$ was examined using the MERLIN instrument at ISIS and its temperature dependence is shown in figure 4.9. A well defined gapped (separated from the ground state) excitation with a bandwidth of $\approx$ 5meV between approximately 15 meV and 20 meV is seen. The observed excita-

tions are specific to the ordering and broadens and weakens at temperatures higher than the 21 K transition temperature. Gapped spin-wave dispersions usually indicate additional terms in the system's spin Hamiltonian which can suggest single-ion anisotropy [69]. In combination with the collinear magnetic order, a one-dimensional Ising model is predicted.

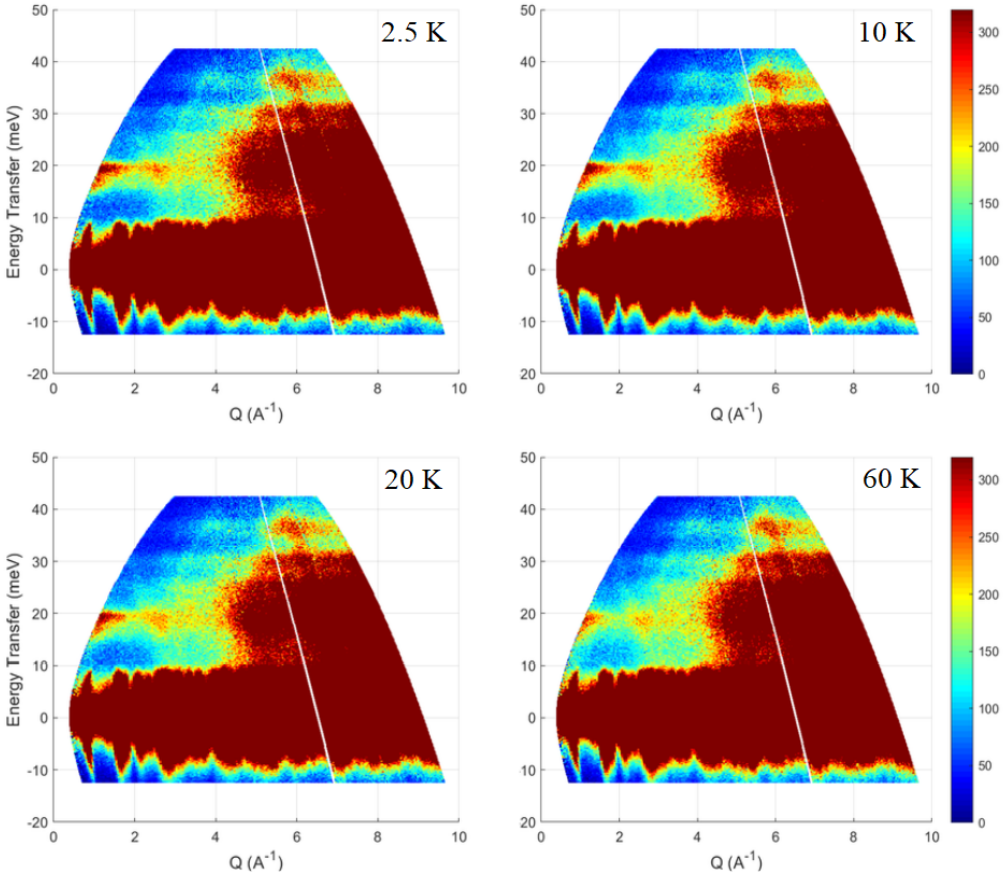

Figure 4.9: Temperature evolution of the magnetic excitation spectrum of $BaMo(PO_4)_2$ measured using the MERLIN instrument at ISIS with neutrons of 50.4meV.

To test the suggested model, analysis using linear spinwave theory was carried out using SpinW [44]. Anticipating exchange and single-ion anisotropy (quantified in D), the spin Hamiltonian, summing over all nearest neighbour spin operators S is:

$$\mathcal{H} = \sum_{i,n} [S^T_{i+1,n} \mathcal{J} + S^T_{i+1,n} \mathcal{J}'] S_{i,n} + \sum_i S^T_i \mathcal{A} S_i \tag{4.4}$$

$$\mathcal{J} = \begin{bmatrix} J_{\mathrm{xy}} & 0 & 0 \\ 0 & J_{\mathrm{xy}} & 0 \\ 0 & 0 & J_{\mathrm{z}} \end{bmatrix} \mathcal{J}' = \begin{bmatrix} J'_{\mathrm{xy}} & 0 & 0 \\ 0 & J'_{\mathrm{xy}} & 0 \\ 0 & 0 & J'_{\mathrm{z}} \end{bmatrix} \mathcal{A} = \begin{bmatrix} 0 & 0 & 0 \\ 0 & 0 & 0 \\ 0 & 0 & D \end{bmatrix} \tag{4.5}$$

The resulting simulated dispersion and fitted model to an energy cut of the collected data are shown in figure 4.10 and 4.11, respectively. The fitted parameters are given in table 4.7. Competing interactions, with $J/J' = 0.80(3)$ suggest a slightly more

one-dimensional system. A relatively large and negative D, indicative of easy-axis single ion anisotropy is observed. This is consistent with the type of anisotropy with another Mo^{4+} material, $La_5Mo_4O_{16}$ [70] and density functional calculations for $BaMo(PO_4)_2$ [71].

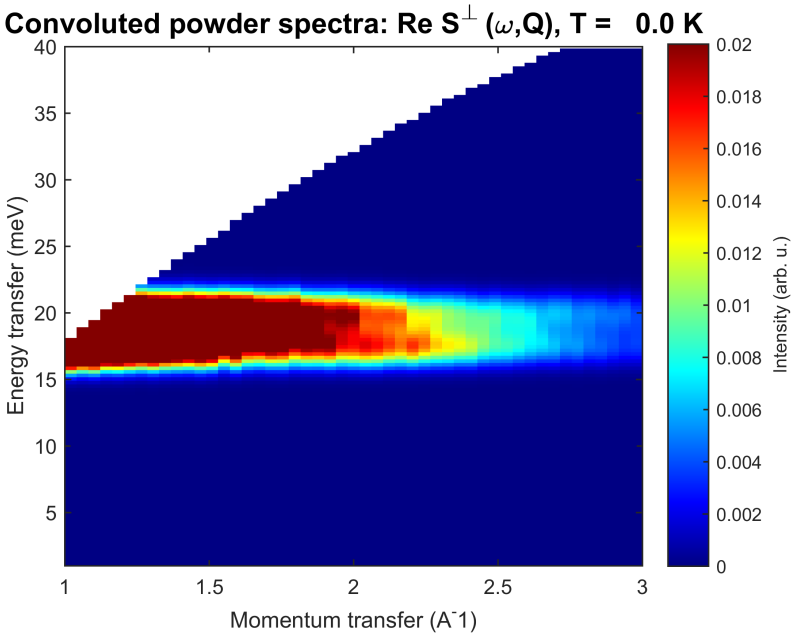

Figure 4.10: Simulated powder-averaged dynamic structure factor S(**Q**,ω) at neutron energy $E = 50.4meV$ and $T = 0K$ with model parameters presented in table 4.7. Qualitative agreement with collected data is seen for 15<E<20 meV excitation in figure 4.9(a).

Table 4.7: Linear spinwave analysis fitting parameters where k_B is Boltzmann constant, and δ signifies the relation $J_{xy} = \delta J_z$ or $J'_{xy} = \delta J'_{xy}$.

J/k_B (K)	25.3(1)
J'/k_B (K)	20.3(1)
D/k_B (K)	76.8(2)
δ	0.570(1)

Further investigation of the complex behavior of BMP is required for an absolute determination of its Hamiltonian. With the available data, several parameter sets were capable of reproducing the dynamic structure factor S(**Q**,ω). The parameter set with the most quantitative and qualitative agreement with the data was presented, which does not completely explain the observed behavior given the fitting $\chi^2 \approx 160$. Numerical simulation of the magnetic susceptibility, derived from the appropriate spin Hamiltonian, would allow for a better approximation of the fitting parameters; this is left for a future work. Limitations were also imposed by the phase of the sample, and a single-crystal would be informative (e.g. direction of anisotropy). Additional experiments such as magnetization could prove valuable in providing a complete set of comparative results.

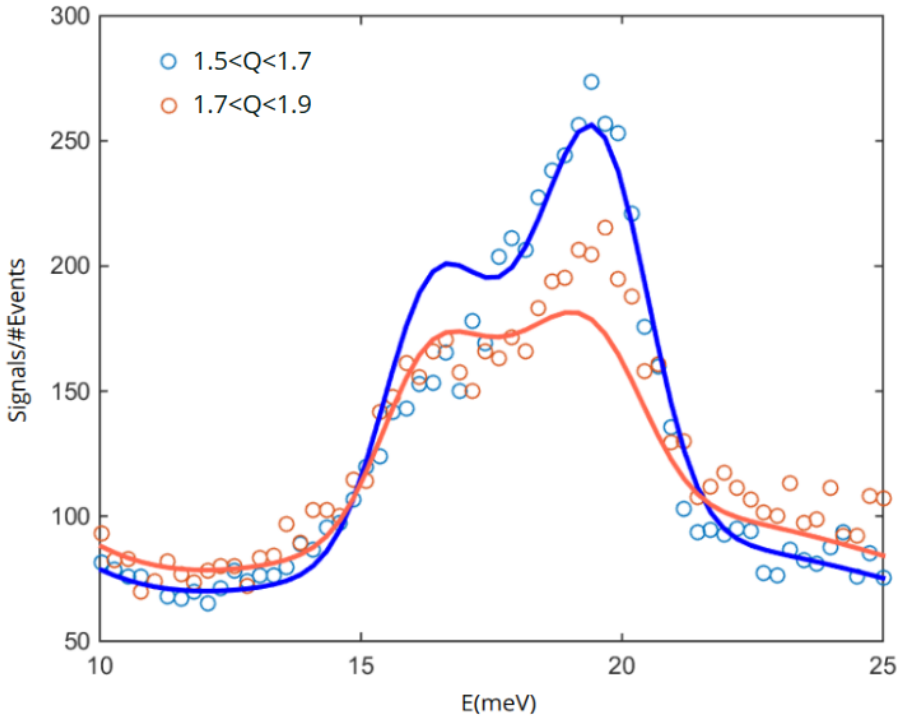

Figure 4.11: Q-integrated intensities for (blue) 1.5<Q<1.7 (orange) 1.7<Q<1.9. Fitting model is shown in solid lines for the respective colors with $\chi^2 \approx 160$.

4.2 $ATi(SO_4)_2$

4.2.1 Nuclear Structure

The crystallographic structures of both $ATi(SO_4)_2$ (A=Rb,Cs) compounds are reported here for the first time. Profile fitting (fig. 4.12) was carried out on PXRD data using the nuclear parameters of isomorphous $KTi(SO_4)_2$ [2]. The resulting unit cell was used as the starting model for Rietveld refinement from which the presence of the desired phases was determined. Structural parameters for both Rb and Cs titanium sulfates are presented in tables 4.8, 4.9, and 4.10. A non-magnetic impurity phase of TiO_2 is present in small amounts (10-15%) in both samples and was found unavoidable following the synthesis route presented in section 3.1.2. Structurally, $ATi(SO_4)_2$ compounds are identical to BMP, and their crystal structure is as that seen in figure 4.3.

A well defined ionic radius trend can be noted in the crystallographic data. The larger the A cation, the more expanded is the unit cell, as expected. This is especially notable when comparing c parameter values. As the strength of superexchange interactions is highly dependent on the distance between Ti-S-O-S-Ti, the increase in unit cell parameters in definite to have an observable effect on the magnetic behavior of both materials.

Table 4.8: PXRD Rietveld refined unit cell parameters at room temperature.

Ion	K [2]	Rb	Cs
a [Å]	8.2894(3)	8.3513(6)	8.4011(5)
b [Å]	5.2257(2)	5.2391(5)	5.2607(4)
c [Å]	7.8441(3)	8.1851(2)	8.6116(4)
β [°]	94.645(2)	95.1407(4)	95.5751(3)

Table 4.9: Resulting crystallographic model for $RbTi(SO_4)_2$ from PXRD data Rietveld refinement at ambient conditions.

Atom	Site	x	y	z	Occ
Rb	2a	0.0000	0.0000	0.0000	1.00
Ti	2c	0.0000	0.0000	0.5000	1.00
S	4i	0.3629(2)	0.0000	0.1956(2)	1.00
O	8j	0.3104(3)	0.0000	0.3838(1)	1.00
O	4i	0.2271(1)	0.0000	0.0579(5)	1.00
O	4i	0.4801(9)	0.2204(4)	0.1837(6)	1.00

Table 4.10: Resulting crystallographic model for $CsTi(SO_4)_2$ from PXRD data Rietveld refinement at ambient conditions.

Atom	Site	x	y	z	Occ
Cs	2a	0.0000	0.0000	0.0000	1.00
Ti	2c	0.0000	0.0000	0.5000	1.00
S	4i	0.3593(6)	0.0000	0.1804(3)	1.00
O	8j	0.3080(4)	0.0000	0.3790(4)	1.00
O	4i	0.2123(4)	0.0000	0.0468(5)	1.00
O	4i	0.4605(3)	0.2073(6)	0.1459(4)	1.00

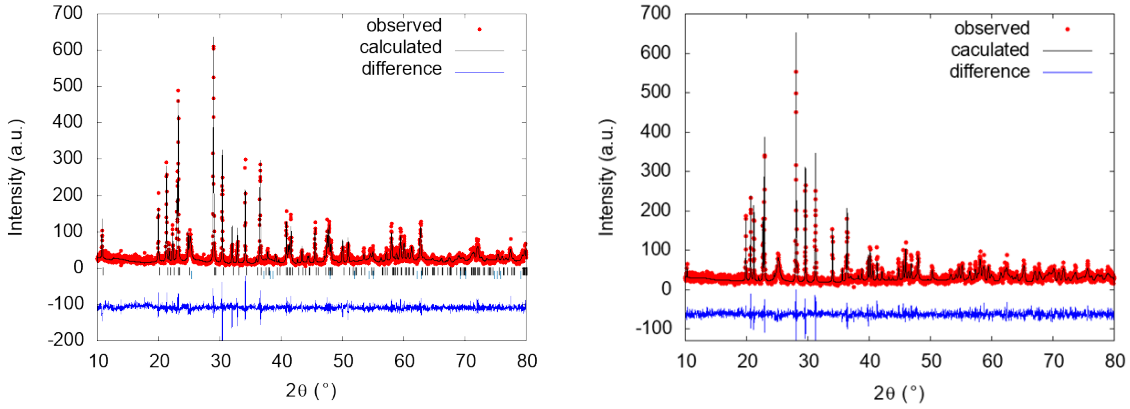

(a) $RbTi(SO_4)_2$ (b) $CsTi(SO_4)_2$

Figure 4.12: LeBail fits of (a) $RbTi(SO_4)_2$ with $\chi^2 = 1.27$ (b) $CsTi(SO_4)_2$ with $\chi^2 = 1.57$ at room temperature.

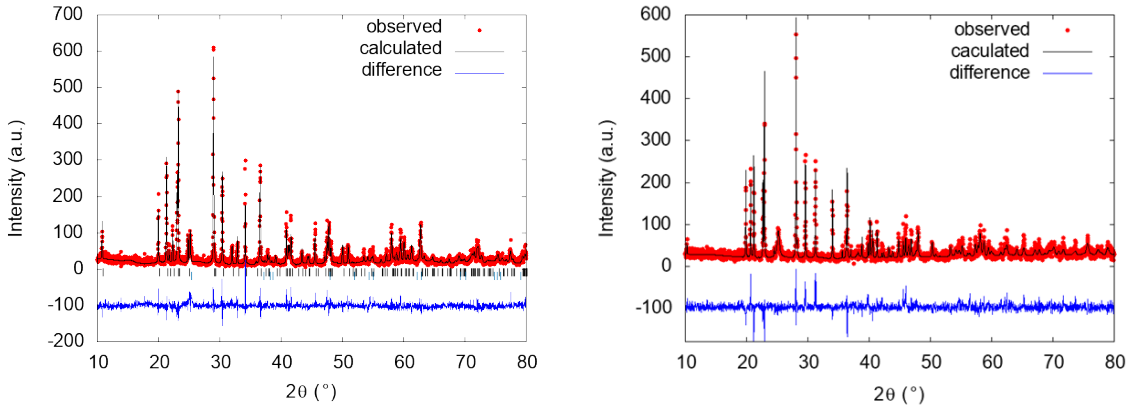

(a) $RbTi(SO_4)_2$ (b) $CsTi(SO_4)_2$

Figure 4.13: PXRD Rietveld refinement of (a) $RbTi(SO_4)_2$ with $\chi^2 = 1.36$ and R_{Bragg}=19.9 (b) $CsTi(SO_4)_2$ with $\chi^2 = 1.79$ and R_{Bragg}=19.1 at room temperature.

4.2.2 Magnetic Properties

Physical property characterization techniques show almost identical low temperature magnetic behavior for all three $S = 1/2$ Ti^{3+} materials. Rb and Cs counterparts to the K [2] compound are thus expected to behave as Heisenberg (3-dimensional spins) one-dimensional chains with NN antiferromagnetic interactions. Anisotropy is not expected to have an effect in the case of Ti^{3+} materials as observed in $KTi(SO_4)_2$ [2]. This is as the strength of LS coupling is much weaker in comparison to Mo^{4+}. For $J' = 0$, this model is dubbed AQHC (antiferromagnetic $S = 1/2$ Heisenberg chain model) [2], and is represented by the spin Hamiltonian on neighbouring $< i, j >$ chain sites as:

$$\mathcal{H}_{AQHC} = J \sum_{<i,j>} S_i.S_j \tag{4.6}$$

Taking geometrical frustration into account adds a perturbation to the spin Hamiltonian such that interactions between different spin chains is accounted for by J'. This model will be called the QHAT ($S = 1/2$ Heisenberg anisotropic triangular lattice) in accordance with [2] and its Hamiltonian is defined as follows:

$$\mathcal{H}_{QHAT} = J \sum_{<i,j>} S_i.S_j + J' \sum_{<i,j>} S_i.S_j \tag{4.7}$$

The temperature dependence of the DC magnetic susceptibility of both $ATi(SO_4)_2$ compounds is shown in figures 4.14 and 4.16. A similar behavior is noted for both substances on a comparable susceptibility scale. A broad feature on both susceptibility curves, characteristic of short-range interactions, can be seen at low temperatures. As seen in figure 4.16, the temperature at which the accumulation of short-range interactions occurs slightly decreases as the ionic radius increases. Paramagnetic tailing is more prominent in $RbTi(SO_4)_2$, indicating a purer $CsTi(SO_4)_2$ sample.

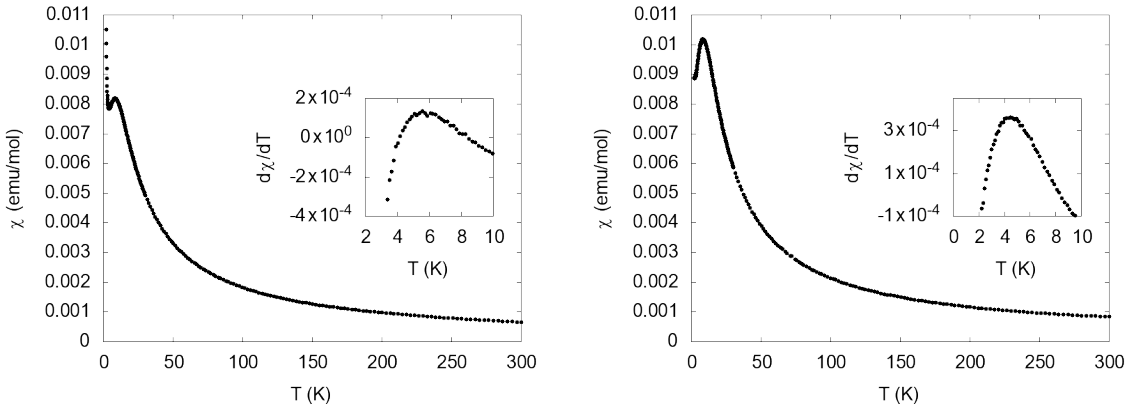

(a) $RbTi(SO_4)_2$ (b) $CsTi(SO_4)_2$

Figure 4.14: DC molar magnetic susceptibility as a function of temperature measured in a 1000 Oe applied magnetic field for (a) $RbTi(SO_4)_2$ (b) $CsTi(SO_4)_2$. Inset: Temperature derivative of magnetic susceptibility as a function of temperature, magnified to the range of expected long-range ordering transition.

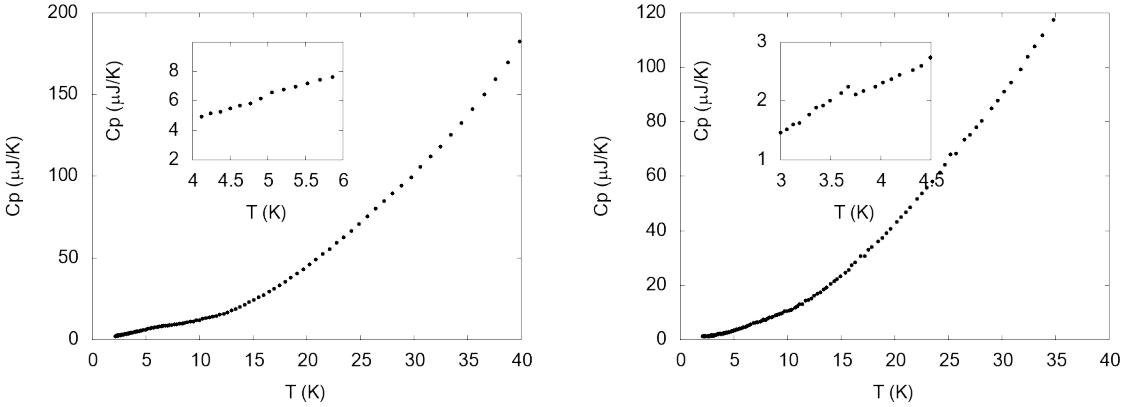

(a) $RbTi(SO_4)_2$ (b) $CsTi(SO_4)_2$

Figure 4.15: ZFC specific heat as a function of temperature for (a) $RbTi(SO_4)_2$ (b) $CsTi(SO_4)_2$. Inset: Magnification at possible weak anomalies in specific heat data indicating possible long-range interactions.

No definite long-range ordering anomalies are noted. This is consistent with $S = 1/2$ low-dimensional systems where the role of quantum fluctuations becomes more pronounced and magnetic ordering is highly suppressed. However, a broad inflection point is observed in both susceptibility curves around 5 K as seen in the inset of figure 4.14 with $d\chi/dT$. Around the same temperature, a very slight feature can be seen in the ZFC specific heat curves of the A=Cs material in figure 4.15. This may be suggestive of weak short-range interactions. However, no clear prediction can be made, as the feature is most probably instrumental. To quantify the differences between the studied materials' magnetic behavior, magnetic susceptibility fits were used. The high temperature behavior (50 K - 300 K) of the magnetic susceptibility is

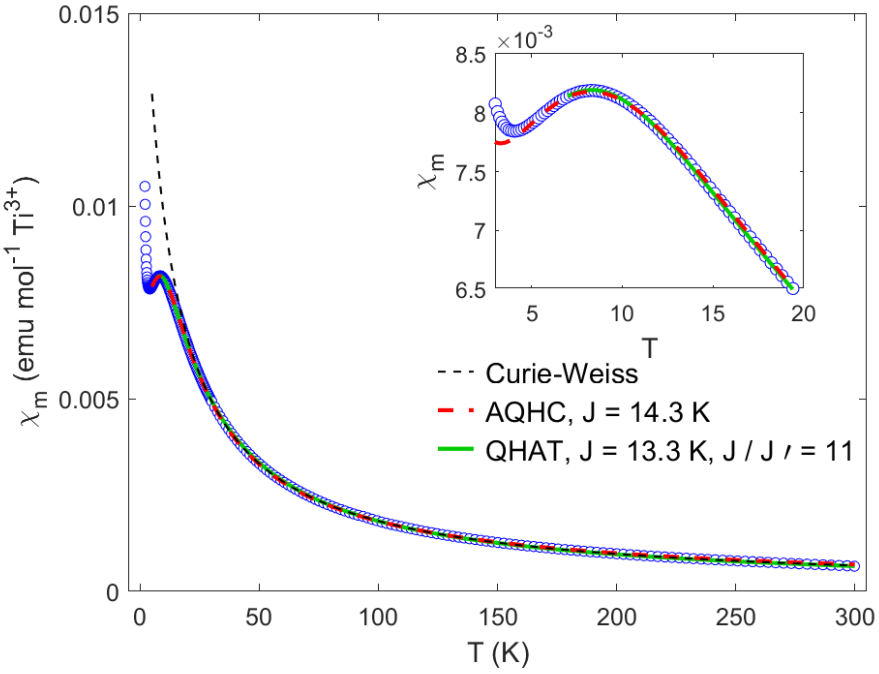

(a) $RbTi(SO_4)_2$

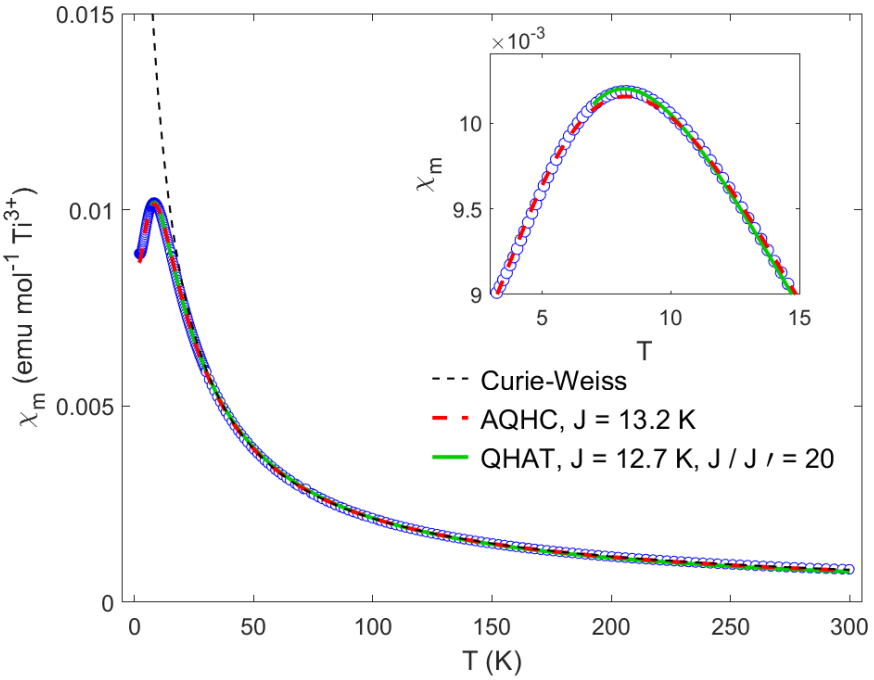

(b) $CsTi(SO_4)_2$

Figure 4.16: Blue circles: DC molar magnetic susceptibility as a function of temperature measured in 1000 Oe applied magnetic field. Dashed black lines: Curie-Weiss model fit according to equation 4.1. Dashed red lines: AQHC model (equation 4.6) fit according to exact diagonalization simulation using ALPS [2, 72]. Green line: QHAT model (equation 4.7) fit using a high-temperature series expansion Padé approximation [73]. Inset: Magnification on the onset of short range interactions.

well defined using the Curie-Weiss expression of equation 4.1 as illustrated in figure 4.15. Fitting parameters are reported in figure 4.17, and a trend of decreasing Weiss constant with increasing crystallographic b parameter is observed. The effective moment decreases in both Rb ($\mu_{eff} = 1.26\mu_B$) and Cs ($\mu_{eff} = 1.31\mu_B$) compounds than its reported value for their potassium counterpart ($\mu_{eff} = 1.68\mu_B$) which may indicate LS coupling.

Testing the AQHC model was completed through susceptibility fits of exact diagonalization results from the ALPS [72] software. Model fit parameters ($\chi^2 \approx 60, 30$ for Rb and Cs, respectively) show a trend of decreasing J strength with increasing b parameter (figure 4.17(b)). This behavior is consistent with the shifting peak position observed in the susceptibility data. The QHAT model was examined using a high temperature series expansion susceptibility expression [73]. Comparatively better fits ($\chi^2 \approx 4, 20$ for Rb and Cs, respectively) than the AQHC model were obtained. A correlation of increasing J/J' with increasing atomic radii is observed as seen in figure 4.17(a). This contradicts the feature indicating possible order in the A=Cs specific heat curve. It should be noted that different starting values for J/J' were used for the model fit, and the parameters best (and lowest χ^2, appendix B) describing the susceptibility curve are the ones presented here.

The resulting trends follow a logical order which can be explained as follows. An increase in J/J' with ionic radius demonstrates an inclination towards one-dimensionality. Given that superexchange distances increase with a growing unit cell, their interaction strengths decline. It is thus apparent that in comparison to J, an already weak J' decreases at a faster rate.

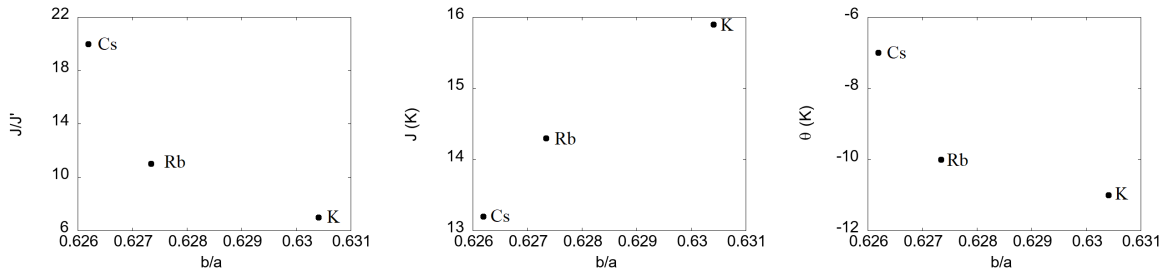

Figure 4.17: Comparative plots indicating of (a) J/J′ (b) J (c) θ_w as a function of crystallographic unit cell parameters b/a suggesting (a) an increase of one-dimensionality (b) decrease in superexchange strength (c) and decrease of Weiss constant θ_w with increasing cation size.

5

Conclusion

The intention of this thesis was to examine the low-temperature magnetic properties of quantum magnets ($S = 1/2, 1$). For that purpose, anisotropic triangular lattices belonging to the anhydrous alum family have been used. The first of these, $BaMo(PO_4)_2$, has been studied using several characterization techniques and its low-temperature properties and spin Hamiltonian are reported here. The synthesis of BMP was carried out using a controlled environment solid-state sintering. Crystallographic information including the desired phase and a paramagnetic impurity are seen and were extracted from the results of Rietveld refinement PXRD and NPD data. Bulk characterization techniques, including magnetic susceptibility and specific heat measurements, suggest an accumulation of short-range interactions at 50 K and antiferromagnetic ordering at a transition temperature of 21 K. From a low-temperature neutron powder diffraction study, the $2a \times 2b \times 2c$ magnetic unit cell is indexed using a $\kappa = (\frac{1}{2}, \frac{1}{2}, \frac{1}{2})$ propagation vector. A suppressed effective moment of $\approx 1.2\mu_B$ results from data refinement, and Ising anisotropy is suggested. Neutron spectroscopy further reveals the role of anisotropy as a gapped excitation of 15meV gap and $\approx 5\ meV$ bandwidth is observed. Using SpinW [44] to quantify the spin Hamiltonian parameters, a quasi two-dimensional Ising Hamiltonian is finally proposed with $J{>}J'$ as relevant to $BaMo(PO_4)_2$.

To study the effect of different ligand cations on the magnetic properties of previously reported $KTi(SO_4)_2$, a series extension of $ATi(SO_4)_2$ (A=Rb,Cs) has been prepared. Synthesis follows a documented hydrothermal route at low temperatures in an autoclave. Nuclear structure determination was carried out utilizing both profile fitting and Rietveld refinement of PXRD data, and a non-magnetic impurity phase of TiO_2 exists in both samples. A well-defined trend of expanding unit cell parameters with ionic radii is observed. At low temperatures, the magnetic properties of all three materials behave similarly with a characteristic onset of short-range interactions occurring between 8 K to 10 K. Minor features below 5 K are seen, but no decisive prediction can be made as they may be instrumental. Magnetic susceptibility fits using expressions of both a Heisenberg one dimensional chain model and a Heisenberg anisotropic triangular lattice were carried out. Both expressions define the susceptibility curves well, with better statistical results for the QHAT model. Trends indicative of increasing one dimensionality with increasing crystallographic b parameter are observed and explained.

Bibliography

1. Momma, K. & Izumi, F. VESTA 3 for three-dimensional visualization of crystal, volumetric and morphology data. English. *Journal of solid state chemistry* **44,** 1272–1276. ISSN: 0021-8898 (DEC 2011).
2. Nilsen, G. J. *et al.* One-dimensional quantum magnetism in the anhydrous alum KTi(SO4)(2). English. *New Journal of Physics* **17.** ISSN: 1367-2630. doi:{10.1088/1367-2630/17/11/113035} (NOV 16 2015).
3. Tokura, Y., Kawasaki, M. & Nagaosa, N. Emergent functions of quantum materials. English. *Nature Physics* **13,** 1056–1068. ISSN: 1745-2473 (Nov 2017).
4. Greedan, J. Geometrically frustrated magnetic materials. English. *Journal of materials chemistry* **11.** 3rd Materials Discussion Meeting of the Royal-Society-of-Chemistry (MD3), Church Coll, Cambridge, England, SEP 26-29, 2000, 37–53. ISSN: 0959-9428 (2001).
5. Balents, L. Spin liquids in frustrated magnets. English. *Nature* **464,** 199–208. ISSN: 0028-0836 (MAR 11 2010).
6. Nayak, C., Simon, S. H., Stern, A., Freedman, M. & Das Sarma, S. Non-Abelian anyons and topological quantum computation. English. *REVIEWS OF MODERN PHYSICS* **80,** 1083–1159. ISSN: 0034-6861 (JUL-SEP 2008).
7. Leonov, A. O. & Mostovoy, M. Multiply periodic states and isolated skyrmions in an anisotropic frustrated magnet. English. *Nature Communications* **6.** ISSN: 2041-1723. doi:{10.1038/ncomms9275} (SEP 2015).
8. Zhou, Y., Kanoda, K. & Ng, T.-K. Quantum spin liquid states. English. *Reviews of Modern Physics* **89.** ISSN: 0034-6861. doi:{10.1103/RevModPhys.89.025003} (APR 18 2017).
9. Mattis, D. *The Theory of Magnetism I: Statics and Dynamics* ISBN: 9783642832383 (Springer Berlin Heidelberg).
10. Cullity, B. & Graham, C. *Introduction to Magnetic Materials* ISBN: 9781118211496 (Wiley, 2011).
11. Blundell, S. *Magnetism in Condensed Matter (Oxford Master Series in Physics)* 1st ed. ISBN: 0198505914 (Oxford University Press, USA, Dec. 2001).
12. Carlin, R. *Magnetochemistry* ISBN: 9783642707339 (Springer Berlin Heidelberg, 2012).
13. Smart, L. & Moore, E. *Solid State Chemistry: An Introduction, Fourth Edition* ISBN: 9781439847923 (CRC Press, 2016).
14. Ressouche, E. Reminder: Magnetic structures description and determination by neutron diffraction. *École thématique de la Société Française de la Neutronique* **13,** 02001 (2014).

15. Tokura, Y. & Kida, N. Dynamical magnetoelectric effects in multiferroic oxides. *Philosophical Transactions of the Royal Society of London A: Mathematical, Physical and Engineering Sciences* **369,** 3679–3694. ISSN: 1364-503X (2011).
16. Stöhr, J. & Siegmann, H. *Magnetism: From Fundamentals to Nanoscale Dynamics* ISBN: 9783540302834 (Springer Berlin Heidelberg, 2007).
17. Maekawa, S. *et al. Physics of Transition Metal Oxides* ISBN: 9783540212935 (Springer Berlin Heidelberg, 2004).
18. Tang, J. & Zhang, P. *Lanthanide Single Molecule Magnets* ISBN: 9783662469996 (Springer Berlin Heidelberg, 2015).
19. Maurice, R. *et al.* Single-Ion Magnetic Anisotropy and Isotropic Magnetic Couplings in the Metal–Organic Framework Fe2(dobdc). *Inorganic Chemistry* **52.** PMID: 23898818, 9379–9389 (2013).
20. Shores, M. P., Nytko, E. A., Bartlett, B. M. & Nocera, D. G. A Structurally Perfect S = 1/2 Kagomé Antiferromagnet. *Journal of the American Chemical Society* **127,** 13462–13463 (2005).
21. Greedan, J., Sato, M., Yan, X. & Razavi, F. Spin-glass-like behavior in Y2Mo2O7, a concentrated, crystalline system with negligible apparent disorder. *Solid State Communications* **59,** 895–897. ISSN: 0038-1098 (1986).
22. Bramwell, S. *et al.* The anhydrous alums as model triangular-lattice magnets. English. *Journal of Physics-Condensed Matter* **8,** L123–L129. ISSN: 0953-8984 (FEB 26 1996).
23. Serrano-Gonzalez, H. *et al.* Magnetic structures of the triangular lattice magnets AFe(SO4)(2) (A = K, Rb, Cs). English. *Journal of applied physics* **83.** 7th Joint Magnetism and Magnetic Materials / International Magnetics Conference, SAN FRANCISCO, CALIFORNIA, JAN 06-09, 1998, 6314–6316. ISSN: 0021-8979 (JUN 1 1998).
24. West, D. V., Huang, Q., Zandbergen, H. W., McQueen, T. M. & Cava, R. J. Structural disorder, octahedral coordination and two-dimensional ferromagnetism in anhydrous alums. English. *Journal of solid state chemistry* **181,** 2768–2775. ISSN: 0022-4596 (OCT 2008).
25. West, D. V. *et al.* PbMn(SO4)(2): A new chiral antiferromagnet. English. *Journal of solid state chemistry* **182,** 2461–2467. ISSN: 0022-4596 (SEP 2009).
26. Tudorache, F. *et al.* Dielectric investigation of (MMIV)-M-II(PO4)(2) double orthophosphates (M-II = Ca, Sr, Ba, Pb; M-IV = Ti, Zr, Hf, Ge, Sn). English. *Journal of alloys and compounds* **509,** 9127–9132. ISSN: 0925-8388 (SEP 15 2011).
27. Hamchaoui, F., Alonzo, V., Venegas-Yazigi, D., Rebbah, H. & Le Fur, E. Six novel transition-metal phosphite compounds, with structure related to yavapaiite: Crystal structures and magnetic and thermal properties of A(I)[M-III(HPO3)(2)] (A=K, NH4, Rb and M=V, Fe). English. *Journal of solid state chemistry* **198,** 295–302. ISSN: 0022-4596 (FEB 2013).
28. Bregiroux, D., Popa, K. & Wallez, G. Crystal chemistry of (MM)-M-II '(IV)(PO4)(2) double monophosphates. English. *Journal of solid state chemistry* **230,** 26–33. ISSN: 0022-4596 (OCT 2015).

29. Miao, C. & Torardi, C. A New High-Efficiency UV-Emitting X-Ray Phosphor, BaHf1xZrx(PO4)2. *Journal of Solid State Chemistry* **155,** 229–232. ISSN: 0022-4596 (2000).
30. Zhao, D. *et al.* Structure twinning, electronic and photoluminescence properties of yavapaiite-type orthophosphate BaTi(PO4)2. *Journal of Physics and Chemistry of Solids* **99,** 59–65. ISSN: 0022-3697 (2016).
31. Morin, E., Wallez, G., Jaulmes, S., Couturier, J. & Quarton, M. Structure of PbIISnIV(PO4)2: Stereochemical Activity of the Lead II Lone Pair. *Journal of Solid State Chemistry* **137,** 283–288. ISSN: 0022-4596 (1998).
32. Bregiroux, D., Wallez, G. & Popa, K. Structural study of polymorphism and thermal behavior of CaZr(PO4)2. *Solid State Sciences* **41,** 43–47. ISSN: 1293-2558 (2015).
33. Popa, K. *et al.* SrNp(PO4)2: an Original Ordered Modification of Cheralite. *Inorganic Chemistry* **49.** PMID: 20608737, 6904–6908 (2010).
34. Fukuda, K., Moriyama, A. & Hashimoto, S. Crystal structure and phase transitions of strontium zirconium diorthophosphate, SrZr(PO4)2. *Journal of Solid State Chemistry* **177,** 3514–3521. ISSN: 0022-4596 (2004).
35. Weller, M., Overton, T., Rourke, J. & Armstrong, F. *Inorganic Chemistry* ISBN: 9780199641826 (OUP Oxford, 2014).
36. Massa, W. & Gould, R. *Crystal Structure Determination* ISBN: 9783540206446 (Springer Berlin Heidelberg).
37. Weller, M., T, M., Young, N. & A, N. *Characterisation Methods in Inorganic Chemistry* ISBN: 9780199654413 (Oxford University Press, 2017).
38. Bragg, W. & Bragg, L. The structure of the diamond. *Proceedings of the Royal Society of London A: Mathematical, Physical and Engineering Sciences* **89,** 277–291. ISSN: 0950-1207 (1913).
39. Taylor, G. The phase problem. *Acta Crystallographica Section D* **59,** 1881–1890 (Nov. 2003).
40. Glusker, J. & Trueblood, K. *Crystal Structure Analysis: A Primer* ISBN: 9780199576340 (OUP Oxford, 2010).
41. Rodríguez-Carvajal, J. Recent advances in magnetic structure determination by neutron powder diffraction. *Physica B: Condensed Matter* **192,** 55–69. ISSN: 0921-4526 (1993).
42. M., R. H. Line profiles of neutron powder-diffraction peaks for structure refinement. *Acta Crystallographica* **22,** 151–152.
43. Bugh, G. *Spin Wave Technology: Initial Release* ISBN: 9780971661615 (Vasant Corporation, 2002).
44. Toth, S. & Lake, B. Linear spin wave theory for single-Q incommensurate magnetic structures. *Journal of Physics-Condensed Matter* **27.** ISSN: 0953-8984. doi:{10.1088/0953-8984/27/16/166002} (APR 29 2015).
45. Rössler, U. *Solid State Theory: An Introduction* ISBN: 9783662099407 (Springer Berlin Heidelberg, 2013).
46. Hippert, F., Geissler, E., Hodeau, J., Lelièvre-Berna, E. & Regnard, J. *Neutron and X-ray Spectroscopy* ISBN: 9781402033377 (Springer Netherlands, 2006).
47. Weinstock, H. *Applications of Superconductivity* ISBN: 9789401707527 (Springer Netherlands, 2013).

48. Clarke, J. & Braginski, A. *The SQUID Handbook: Fundamentals and Technology of SQUIDs and SQUID Systems* ISBN: 9783527604586. https://books.google.se/books?id=BsTTM-nU-JkC (Wiley, 2006).
49. Fagaly, R. SQUID Instruments and Applications. *Review of Scientific Instruments* (2005).
50. Nave, R. *SQUID Magnetometer and Josephson Junctions* http://hyperphysics.phy-astr.gsu.edu/hbase/Solids/Squid.html (2018).
51. Kittel, C. *Introduction to Solid State Physics* ISBN: 9780471415268 (Wiley, 2004).
52. Tanner, B. *Introduction to the Physics of Electrons in Solids* ISBN: 9780521239417. https://books.google.se/books?id=0WBfQgAACAAJ (Cambridge University Press, 1995).
53. Ventura, G. & Perfetti, M. *Thermal Properties of Solids at Room and Cryogenic Temperatures* ISBN: 9789401789691 (Springer Netherlands, 2014).
54. Toby, B. R Factors in Rietveld Analysis: How Good is Good Enough. **21** (Mar. 2006).
55. Young, R. *The Rietveld Method* ISBN: 9780198559122 (Oxford University Press, 1995).
56. Perl, J., Shin, J., Schumann, J., Faddegon, B. & Paganetti, H. TOPAS: An innovative proton Monte Carlo platform for research and clinical applications. *Medical Physics* **39,** 6818 (2012).
57. Rodriguez-Carvajal, J. *FULLPROF: a program for Rietveld refinement and pattern matching analysis* in *satellite meeting on powder diffraction of the XV congress of the IUCr* **127** (1990).
58. Bail, A. L., Duroy, H. & Fourquet, J. Ab-initio structure determination of LiSbWO6 by X-ray powder diffraction. *Materials Research Bulletin* **23,** 447–452. ISSN: 0025-5408 (1988).
59. Pawley, G. S. Unit-cell refinement from powder diffraction scans. *Journal of Applied Crystallography* **14,** 357–361 (Dec. 1981).
60. Chateigner, D. *Combined Analysis* ISBN: 9781118622643 (Wiley, 2013).
61. Le Bail, A. *et al. Powder Diffraction. Theory and Practice* (eds Dinnebier, R. E. & Billinge, S. J. L.) p134–p165. ISBN: 978-0-85404-231-9. doi:10.1039/9781847558237 (The Royal Society of Chemistry, 2008).
62. Ibberson, R. M. Design and performance of the new supermirror guide on HRPD at ISIS. *Nuclear Instruments and Methods in Physics Research Section A: Accelerators, Spectrometers, Detectors and Associated Equipment* **600,** 47–49. ISSN: 0168-9002 (2009).
63. C. Chapon, L. *et al.* Wish: The New Powder and Single Crystal Magnetic Diffractometer on the Second Target Station. **22,** 22–25 (Apr. 2011).
64. Arnold, O. *et al.* Mantid—Data analysis and visualization package for neutron scattering and SR experiments. *Nuclear Instruments and Methods in Physics Research Section A: Accelerators, Spectrometers, Detectors and Associated Equipment* **764,** 156–166. ISSN: 0168-9002 (2014).
65. Bewley, R. I. *et al.* MERLIN, a new high count rate spectrometer at ISIS. English. *PHYSICA B-CONDENSED MATTER* **385-86.** 8th International Con-

ference on Neutron Scattering, Sydney, AUSTRALIA, NOV 27-DEC 02, 2005, 1029–1031. ISSN: 0921-4526 (NOV 15 2006).

66. Leclaire, A., Barel, M., Chardon, J. & Raveau, B. A Mo(IV) Monophosphate, BaMo(PO4)2, with the Yavapaiite Layer Structure. *Journal of Solid State Chemistry* **116,** 364–368. ISSN: 0022-4596 (1995).
67. Khilla, M. A., Mikhail, H., Abu-El Soud, A. & Hanafi, Z. M. Magnetic susceptibility of molybdenum trioxide, dioxide and some suboxides. *Czechoslovak Journal of Physics B* **30,** 1039–1045. ISSN: 1572-9486 (Sept. 1980).
68. Perez-Mato, J. *et al.* Symmetry-Based Computational Tools for Magnetic Crystallography. *Annual Review of Materials Research* **45,** 217–248 (2015).
69. Rotter, M., Le, M. D., Boothroyd, A. & Blanco, J. Dynamical matrix diagonalization for the calculation of dispersive excitations. **24,** 213201 (May 2012).
70. Iida, K. *et al.* Time-of-Flight Elastic and Inelastic Neutron Scattering Studies on the Localized 4d Electron Layered Perovskite La5Mo4O16. *Journal of the Physical Society of Japan* **86,** 064803 (2017).
71. Hembacher, J. *et al.* Stripe order and magnetic anisotropy in the $S = 1$ antiferromagnet $BaMoP_2O_8$ (June 2018).
72. Bauer, B. *et al.* The ALPS project release 2.0: open source software for strongly correlated systems. English. *Journal of Statistical Mechanics-Theory and Experiment.* ISSN: 1742-5468. doi:{10.1088/1742-5468/2011/05/P05001} (May 2011).
73. Zheng, W., Singh, R. R. P., McKenzie, R. H. & Coldea, R. Temperature dependence of the magnetic susceptibility for triangular-lattice antiferromagnets with spatially anisotropic exchange constants. *Phys. Rev. B* **71,** 134422 (13 Apr. 2005).
74. Singh, P., Shiva, K., Celio, H. & Goodenough, J. B. Eldfellite, NaFe(SO4)(2): an intercalation cathode host for low-cost Na-ion batteries. English. *Energy & environmental science* **8,** 3000–3005. ISSN: 1754-5692 (2015).

A

Appendix A

NFS was prepared following the procedure outlined by Singh [74], where the reaction is:

$$NH_4Fe(SO_4)_2 + NaHCO_3 \longrightarrow NaFe(SO_4)_2 + CO_2 + H_2O + NH_3 \qquad (A.1)$$

A stoichiometric amount of $NH_4Fe(SO_4)$ (Alfa Aesar 97-100%) and $NaHCO_3$ (Alfa Aesar 98%) is dissolved in water with constant stirring. The product immediately forms as a light orange precipitate. The solution is heated at 80°C for water evaporation, and the precipitate is collected for grinding, pelletizing, and two annealing stages at 200°C/12h and 350°C/24h in an alumina crucible. Monitoring the concentration of the reactants is essential as the product's purity is highly sensitive to the stoichiometry.

The magnetic susceptibility and specific heat curves collected using the methods outlined in chapter 3 are presented in figure A.1.

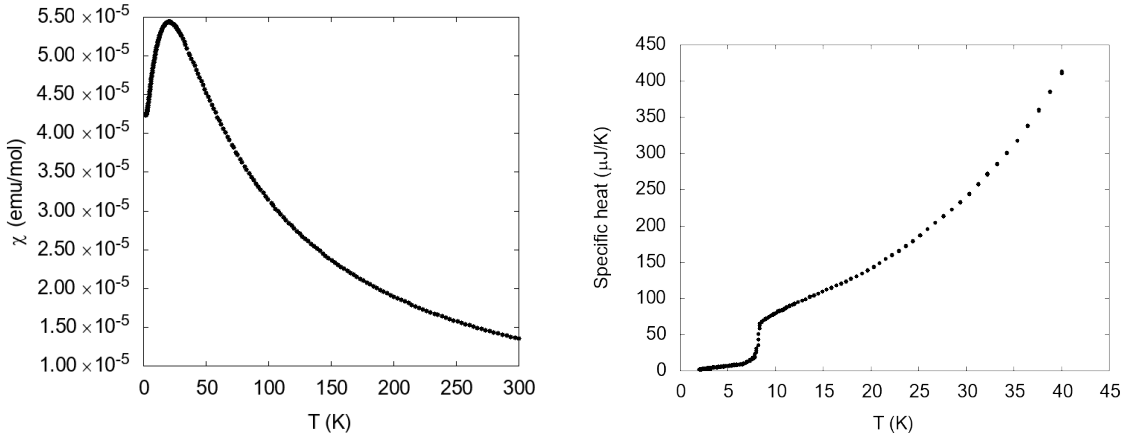

(a) Molar magnetic susceptibility (b) Specific heat

Figure A.1: (a) DC molar magnetic susceptibility as a function of temperature measured in a 1000 Oe applied magnetic field. (b) ZFC specific heat as a function of temperature.

Neutron powder diffraction studies were carried out using both the HRPD and WISH instruments. Using the data collected from HRPD, the nuclear structure was determined using Rietveld refinement (fig A.2). Refinement crystallographic results

are presented in tables A.1 and A.2. Low temperature neutron powder diffraction data was collected using WISH and is presented in figure A.3. A multitude of magnetic Bragg peaks is noted upon subtracting high and low temperature data, and no analysis has been yet completed.

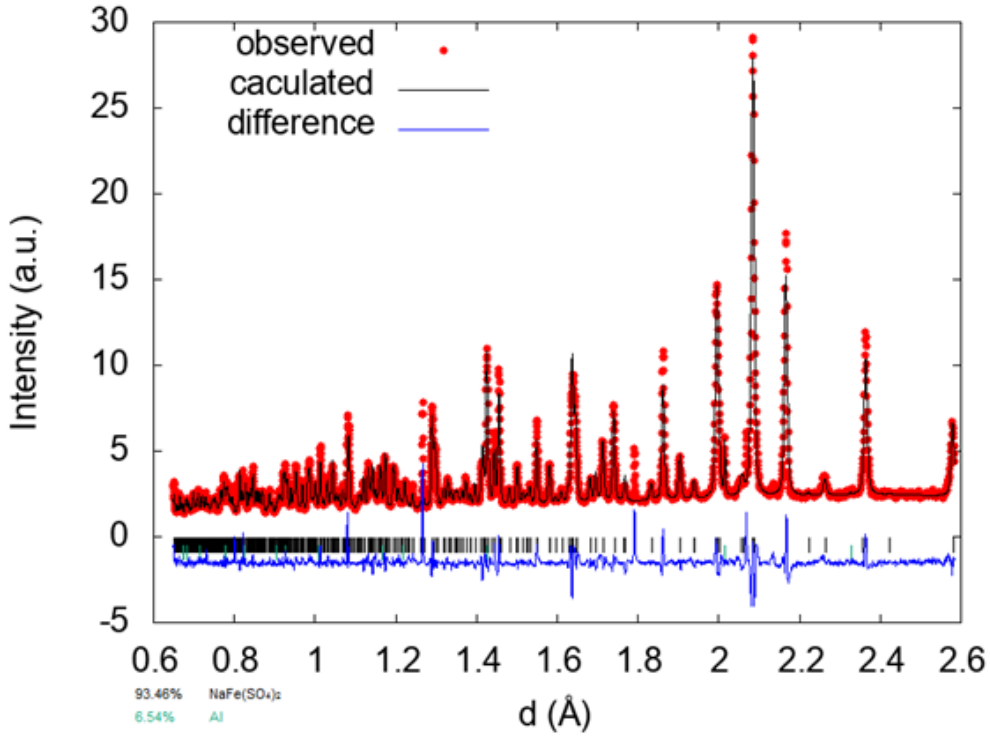

Figure A.2: $NaFe(SO_4)_2$ NPD Rietveld refinement on HRPD.

Table A.1: $NaFe(SO_4)_2$ refined unit cell parameters. R_p=1.63

a [Å]	7.9777(2)
b [Å]	5.1530(1)
c [Å]	7.0670(2)
β [°]	91.9387(2)

Table A.2: Refined crystallographic information for $NaFe(SO_4)_2$ on HRPD.

Atom	Site	x	y	z	Occ	B_{iso}
Na	2a	0.0000	0.0000	0.5000	1.00	0.21(1)
Fe	2c	0.0000	0.0000	0.0000	1.00	0.14(1)
S	4i	0.3584(4)	0.0000	0.2245(2)	1.00	1.10 (6)
O	8j	0.4706(1)	0.2343(1)	0.2047(1)	1.00	0.54(2)
O	4i	0.2384(2)	0.0000	0.0598(1)	1.00	0.10(3)
O	4i	0.2875(2)	0.0000	0.4061(2)	1.00	0.67(3)

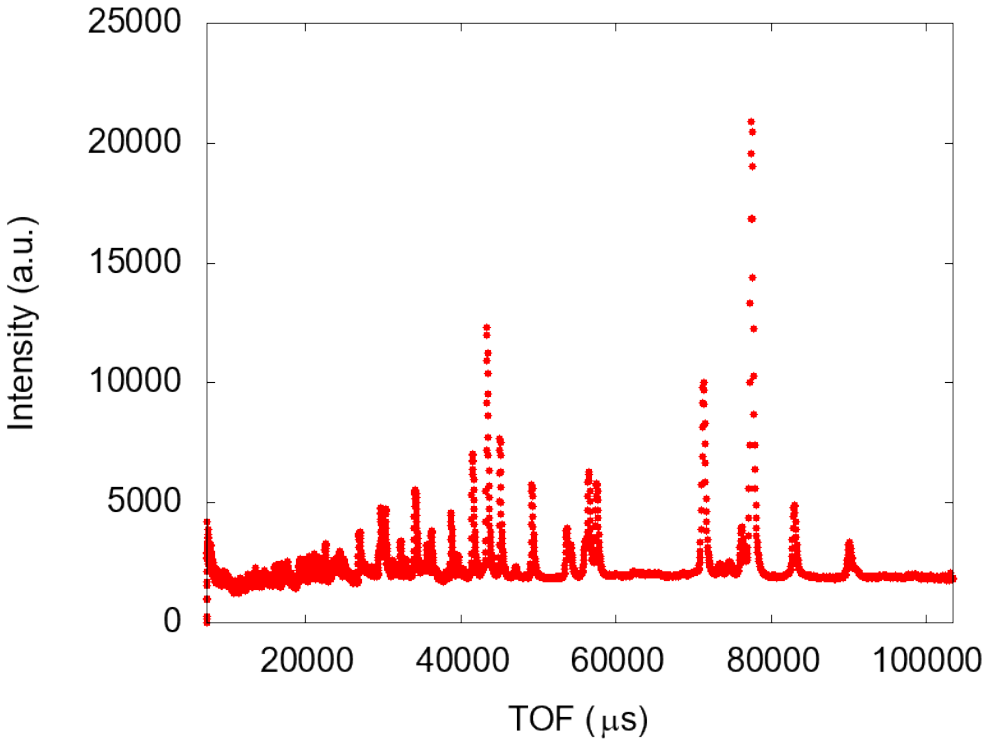

Figure A.3: $NaFe(SO_4)_2$ NPD diffractogram at 1.5K on WISH.

B

Appendix B

B.1 Supplementary Results

For the QHAT susceptibility expression fit of $ATi(SO_4)_2$ (A=Rb,Cs), the presented results are given for the starting parameters giving the lowest χ^2 statistic and best qualitative agreement with data. As can be seen in figures x and y, for both materials, χ^2 sharply increases as J/J' goes below 7, with completely inconsistent fits below 5.

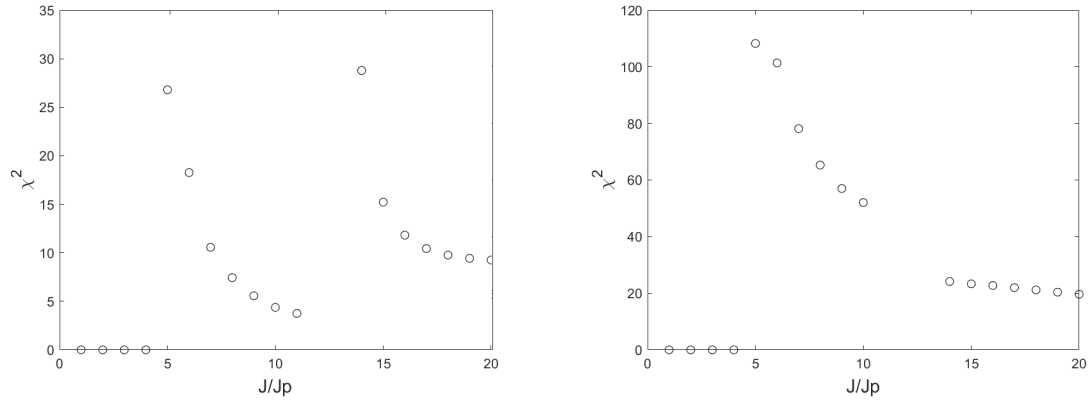

(a) $RbTi(SO_4)_2$ (b) $CsTi(SO_4)_2$

Figure B.1: The dependence of χ^2 on the starting J/J' parameter for QHAT model susceptibility fits.